



## Steady extrusion of viscoelastic materials from an annular die

George Karapetsas, John Tsamopoulos\*

Laboratory of Computational Fluid Dynamics, Department of Chemical Engineering, University of Patras, Patras 26500, Greece

### ARTICLE INFO

#### Article history:

Received 30 November 2007

Received in revised form 16 April 2008

Accepted 17 April 2008

#### Keywords:

Annular flow

Polymer extrusion

Viscoelastic fluids

Free surface flows

### ABSTRACT

The steady extrusion of viscoelastic materials from a straight, annular die is studied theoretically. The viscoelastic behavior is modelled using the affine Phan-Thien and Tanner (PTT) constitutive equation of the exponential form. For the numerical solution of the governing equations the mixed finite element method is combined with a quasi-elliptic mesh generation scheme in order to capture the large deformations of the two free surfaces of the extrudate. The elastic-viscous stress splitting technique (EVSS-G) is used to separate the elastic and viscous contributions to the polymeric part of the stress tensor together with a streamline upwind Petrov-Galerkin (SUPG) weighting for the discretization of the constitutive equation. This combination of solution methods and constitutive model allows us (i) to compute accurate steady-state solutions up to very high Weissenberg numbers resulting in very high deformations of the free surfaces (ii) construct and store the Jacobian matrix, which is necessary to conduct linear stability analysis for this flow. First, results for the fully developed flow of a PTT liquid inside an annular die are presented. They reveal a complex interplay between material elasticity, shear thinning and solvent viscosity. Next, a complete parametric analysis of annular extrusion is performed. Such a complete study using the PTT model has not been reported before, even at much lower  $Wi$  numbers. It is found that swelling of the material increases sharply up to moderate Weissenberg numbers, whereas its rate of increase is reduced for higher values of  $Wi$ , as shear thinning becomes increasingly important. The latter generally plays a crucial role, in addition to elasticity, on the swelling of the extrudate. Moreover, as the contribution of the solvent viscosity increases, the contribution of elastic stresses decreases causing a decrease in the swelling of the material which approaches the Newtonian limit. The predicted swelling ratios, which characterize the geometry of the extrudate, are in satisfactory agreement with earlier experimental and theoretical data for three particular HDPE resins.

© 2008 Elsevier B.V. All rights reserved.

### 1. Introduction

The steady extrusion of a viscoelastic liquid through an annular die is an important engineering process, since it has many applications in the polymer processing industry including production of pipes, of annular preforms to be used in blow molding and of annular films to be used in film blowing and wire coating. As it is widely known, when a viscoelastic fluid is extruded through a slit, a cylindrical or an annular die, it experiences significant swelling. This is caused mainly by the relaxation of the polymeric chains, which, from being oriented primarily in the flow direction inside the die, can relax to any configuration outside it, where the flow field is completely rearranged. Since in most applications accurate dimensions of the extruded products are required, the level of swelling that the fluid experiences is an important design parameter. Therefore the annular extrusion process has been the subject of several

publications in the past. Next we will mention briefly only those that seem to be most relevant to the present study.

A nice review on the experimental efforts that have been carried out by various groups to study the annular extrusion has been given by Garcia-Rejon et al. [1]. Pearson and Trottnow [2] were the first to attempt to address this problem theoretically following the ideas of Tanner [3] for the capillary die swell. A theoretical study of this problem has been reported by Crochet and Keunings [4]. They were the first to simulate the extrusion of a non-Newtonian fluid using the finite element method to solve the flow of a Maxwell fluid exhibiting, however, only small elastic effects. More recently, Luo and Mitsoulis [5] presented streamline finite element (SFEM) calculations, using the K-BKZ integral model, for a viscoelastic fluid flowing through straight, converging and diverging annular dies. Garcia-Rejon et al. [1] used the same viscoelastic model also to study the effect of the die geometry on the annular swell, although they employed the finite element method combined with the inconsistent  $SU4 \times 4$  method proposed by Marchal and Crochet [6]. The annular flow of a power-law and a second order fluid was studied by Seo [7], while shortly after Ahn and Ryan [8]

\* Corresponding author. Fax: +30 2610 996 178.

E-mail address: [tsamo@chemeng.upatras.gr](mailto:tsamo@chemeng.upatras.gr) (J. Tsamopoulos).

used a finite difference scheme to study the flow of a power-law fluid. Tanoue et al. [9] performed viscoelastic simulations using the Giesekus model reaching high values of the Weissenberg number, although in order to achieve that, they also employed the inconsistent SU4  $\times$  4 method. Subsequently, Tanoue and Iemoto [10] used the same method to study the effect of different annular die geometries on the flow of a Giesekus fluid. The SFEM method was also used to perform simulations for the HDPE using various viscoelastic models by Otsuki et al. [11,12]. Very recently, Mitsoulis [13] presented simulations using the regularized Herschel-Bulkley or the power-law fluid models to study the extrusion of pseudoplastic or viscoplastic fluids. The effect of surface tension and gravity acting in the flow direction on the steady annular extrusion, which could become important at small flow rates but was neglected by most researchers until then, was studied by Housiadas et al. [14] for a Newtonian fluid. The same two forces were retained also by Housiadas and Tsamopoulos [15,16], who used the thin film approximation to study the transient extrusion of annular films obeying the Oldroyd-B fluid model. More recently, Georgiou [17] presented simulations to study the effect of inertia at high Reynolds numbers on the shape of the extrudate for a Newtonian fluid.

Two are the main objectives of this paper (i) to develop an accurate and efficient numerical method in order to solve the axisymmetric and steady extrusion of a viscoelastic material following a widely accepted differential constitutive model from an annular die and perform an extensive parametric analysis to study the effect of model parameters on the shape of the extrudate and (ii) to do so in a way that the Jacobian matrix of the entire problem is generated which would be necessary in order to perform a linear stability analysis of this problem, an unresolved problem until now. The hyperbolic nature of the constitutive equations requires the values of the elastic stresses far enough inside the die as initial conditions for the two-dimensional calculations. This necessitates calculating the elastic stresses for the fully developed annular flow. To our surprise, results for this kind of flow of an exponential PTT fluid model with or without a solvent viscosity have not been reported before. In the two-dimensional numerical simulations, we use the finite element method combined with an elliptic grid generation scheme for the calculation of the unknown positions of the inner and outer free surfaces; see Dimakopoulos and Tsamopoulos [18]. We have applied this method to a number of free or moving boundary problems, such as the transient squeeze of a viscoplastic material between parallel disks, Karapetsas and Tsamopoulos [19]; the displacement of a Newtonian, a viscoelastic or a viscoplastic fluid from a tube, Dimakopoulos and Tsamopoulos [20–22]; the deformation and displacement of several bubbles inside a filament undergoing stretching, Foteinopoulou et al. [23] and the steady bubble rise and entrapment in Bingham fluids, Tsamopoulos et al. [24].

The rest of the paper is organized as follows. In Section 2, we present the governing equations and the boundary conditions for this problem. The numerical algorithm, used in our calculations, is briefly described in Section 3. In Section 4, we present the results of the extensive parametric analysis that we performed for a viscoelastic fluid undergoing either fully developed flow inside the annular die or flow inside the die and extrusion from it. Finally concluding remarks are made in Section 5.

## 2. Problem formulation

We consider the steady, axisymmetric flow of a viscoelastic fluid as it is extruded from an annular die. The fluid is incompressible with constant density  $\rho$ , relaxation time  $\lambda$  and total dynamic viscosity  $\mu = \mu_s + \mu_p$ , where  $\mu_s$  and  $\mu_p$  are the viscosities of the solvent

and the polymer, respectively. The flow geometry, which is examined here, is depicted in Fig. 1. The viscoelastic fluid flows inside an annular die of inner radius  $R_i$ , outer radius  $R_o$  and length  $L_1$  and as it exits from the die it swells and rearranges its shape. The fluid motion is simulated until far from the die exit, at distance  $L_2$ , the flow becomes fully developed. There, the inner and outer radii of the material are  $H_1$  and  $H_2$ , respectively.

We scale all lengths with the outer radius of the annular die,  $R_o$ , and velocities with the mean velocity,  $V$ , at the die entrance. In addition both the pressure and stress components are scaled with a viscous scale,  $\mu V/R_o$ . Thus, the dimensionless groups that arise are the Reynolds number,  $Re = \rho V R_o/\mu$ , the Weissenberg number,  $Wi = \lambda V/R_o$ , the ratio of the solvent viscosity over the total viscosity,  $\beta = \mu_s/\mu$ , and the geometric ratios  $l_1 = L_1/R_o$ ,  $l_2 = L_2/R_o$ ,  $h_1 = H_1/R_o$ ,  $h_o = H_o/R_o$  and  $a = R_i/R_o$ .

Inserting the previously defined characteristic quantities into the radial and axial momentum balances and the mass conservation equation, we obtain:

$$Re \underline{v} \cdot \underline{\nabla} \underline{v} + \underline{\nabla} P - \underline{\nabla} \cdot \underline{\underline{\tau}} = 0 \quad (1)$$

$$\underline{\nabla} \cdot \underline{v} = 0 \quad (2)$$

where  $\underline{\nabla}$  denotes the gradient operator for cylindrical coordinates,  $\underline{v}$  and  $P$  are the axisymmetric velocity and pressure fields, respectively, and  $\underline{\underline{\tau}}$  is the extra stress tensor, which is split into a purely viscous part,  $2\beta \underline{\underline{\dot{\gamma}}}$  and a polymeric contribution  $\underline{\underline{\tau}}_p$ :

$$\underline{\underline{\tau}} = 2\beta \underline{\underline{\dot{\gamma}}} + \underline{\underline{\tau}}_p \quad (3)$$

where  $\underline{\underline{\dot{\gamma}}}$  is the rate-of-strain tensor defined as  $\underline{\underline{\dot{\gamma}}} = 1/2(\underline{\nabla} \underline{v} + \underline{\nabla} \underline{v}^T)$ .

To complete the description, a constitutive equation that describes the rheology of the fluid is required in order to determine the polymeric part of the extra stress tensor. As such we use the following differential model that has been proposed by Phan-Thien and Tanner [25].

$$Y(\underline{\underline{\tau}}_p) \underline{\underline{\tau}}_p + Wi \underline{\underline{\dot{\tau}}}_p^\diamond - 2(1 - \beta) \underline{\underline{\dot{\gamma}}} = 0 \quad (4)$$

where the symbol  $\diamond$  over the viscoelastic stress denotes the Gordon–Schowalter derivative defined as

$$\underline{\underline{\dot{X}}} = \frac{DX}{Dt} - (\underline{\nabla} \underline{v} - \xi_s \underline{\underline{\dot{\gamma}}})^T \cdot \underline{\underline{X}} - \underline{\underline{X}} \cdot (\underline{\nabla} \underline{v} - \xi_s \underline{\underline{\dot{\gamma}}}) \quad (5)$$

where  $\underline{\underline{X}}$  is any second order tensor. Two forms of the PTT model are in common use, namely the linearized form [25], where the function  $Y(\underline{\underline{\tau}}_p)$  is

$$Y(\underline{\underline{\tau}}_p) = 1 + \frac{\varepsilon}{1 - \beta} Wi tr \underline{\underline{\tau}}_p \quad (6a)$$

and the exponential form [26] with

$$Y(\underline{\underline{\tau}}_p) = \exp \left[ \frac{\varepsilon}{1 - \beta} Wi tr \underline{\underline{\tau}}_p \right] \quad (6b)$$

The linearized form of this model has been used successfully by Luo and Tanner [27] in simulating extrusion of a viscoelastic material from either a planar or a cylindrical (axisymmetric) die up to relatively high  $Wi$  numbers. In our simulations we have used the exponential form of the PTT model. Both PTT models have two parameters,  $\xi_s$  and  $\varepsilon$ . The first one is related to the non-affine motion of the polymer chains with respect to the macroscopic motion of the continuum. By setting  $\xi_s$  equal to zero no such motion or slip is allowed, the Gordon–Schowalter derivative reduces to the upper convective one and the fluid model is referred to as the affine PTT model. The other parameter,  $\varepsilon$ , imposes an upper limit to the elongational viscosity, which increases as this parameter decreases, while it introduces elongational thinning. Moreover  $\varepsilon$  is related to

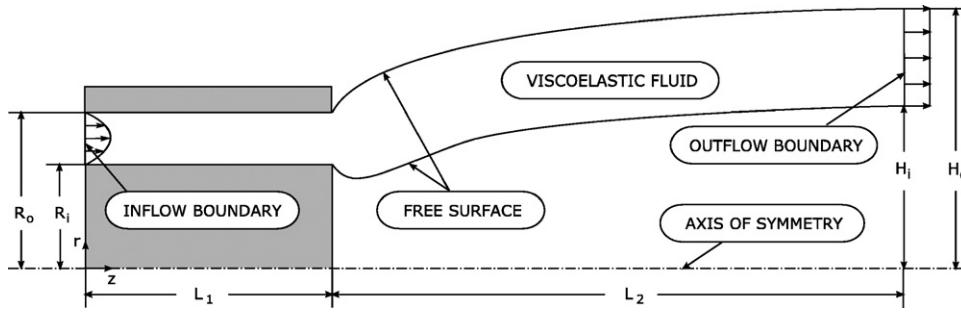


Fig. 1. Schematic of the flow geometry and coordinate system.

the shear-thinning behavior of the model. Clearly, the PTT model reduces to the OLDROYD-B model by setting both  $\varepsilon = 0$  and  $\xi_s = 0$ . Retaining the zero values for  $\varepsilon$  and  $\xi_s$  and additionally setting  $\beta = 0$ , the PTT model reduces to the UCM model.

In order to solve accurately and efficiently various viscoelastic flows Rajagopalan et al. [28] introduced the elastic-viscous split stress (EVSS) formulation. This method consists of splitting the polymeric part of the extra stress tensor into a purely elastic and a viscous part

$$\underline{\underline{\tau}}_p = \underline{\underline{\Sigma}} + 2(1 - \beta)\dot{\underline{\underline{\gamma}}}_e \quad (7)$$

The success of this scheme resides on the fact that the elliptic nature of the momentum equations is ensured even for  $\beta = 0$ . Brown et al. [29] proposed a modification of this idea, called EVSS-G, according to which an independent (continuous) interpolation,  $\underline{\underline{G}}$ , of the components of the (discontinuous, if calculated from the velocity FE interpolation) velocity gradient tensor,  $\nabla \underline{\underline{v}}$ , is introduced wherever the latter arises in the constitutive equation. Thus compatibility in the finite element representation between elastic stress,  $\underline{\underline{\Sigma}}$ , and  $\underline{\underline{G}}$  in the constitutive equation is achieved, even where the velocity vector reduces to zero. This is particularly important for the terms involving spatial derivatives of  $\nabla \underline{\underline{v}}$ , which are substituted with derivatives of  $\underline{\underline{G}}$ . The additional equation that must be solved is

$$\underline{\underline{G}} = \nabla \underline{\underline{v}} \quad (8)$$

Thus after reformulating the momentum and constitutive equations using the EVSS-G formulation we obtain

$$Re \underline{\underline{v}} \cdot \nabla \underline{\underline{v}} + \nabla P - \nabla \cdot \underline{\underline{\Sigma}} - 2 \nabla \cdot \dot{\underline{\underline{\gamma}}}_e = 0 \quad (9)$$

$$Y(\underline{\underline{\tau}}_p) \underline{\underline{\Sigma}} + Wi \underline{\underline{\Sigma}} + 2Wi(1 - \beta) \underline{\underline{D}} - 2(1 - \beta)(1 - Y(\underline{\underline{\tau}}_p)) \underline{\underline{D}} = 0 \quad (10)$$

where  $\underline{\underline{D}} = 1/2(\underline{\underline{G}} + \underline{\underline{G}}^T)$ . Moreover the definition of the Gordon–Schowalter derivative becomes

$$\overset{\diamond}{\underline{\underline{X}}} = \frac{D \underline{\underline{X}}}{Dt} - (\underline{\underline{G}} - \xi_s \underline{\underline{D}})^T \cdot \underline{\underline{X}} - \underline{\underline{X}} \cdot (\underline{\underline{G}} - \xi_s \underline{\underline{D}}) \quad (11)$$

Along the free surfaces of the fluid, we ignore the effect of surface tension, since in most viscoelastic flows it is rather negligible. Therefore the force balance equation, after setting the pressure in the surrounding fluid to zero (datum pressure), becomes

$$\underline{\underline{n}} \cdot (-P \underline{\underline{I}} + \underline{\underline{\tau}}) = 0 \quad (12)$$

where  $\underline{\underline{n}}$  is the outward unit normal to the free surface. Moreover, the velocity component normal to this free surface is zero

$$\underline{\underline{n}} \cdot \underline{\underline{v}} = 0 \quad (13)$$

On both walls of the annular die ( $r = a, r = 1$  and  $0 \leq z \leq l_1$ ) we impose the usual no-slip and no-penetration conditions

$$v_r = 0, \quad v_z = 0 \quad (14)$$

Boundary conditions must be also applied at the entrance of the die and at the outflow boundary. We consider that both boundaries are far enough from the die exit and thus we can assume that the flow there is fully developed. Therefore at the outflow boundary ( $z = l_1 + l_2$ ) we impose the following conditions of fully developed plug flow

$$v_r = 0 \quad (15)$$

$$\frac{\partial v_z}{\partial z} = 0 \quad (16)$$

At the die entrance ( $z = 0$ ), besides the boundary conditions for the velocity we also have to apply boundary conditions for the polymeric part of the stresses due to the hyperbolic character of the constitutive equation. Since the flow there is fully developed, the radial velocity is equal to zero,  $v_r = 0$ , while the axial velocity as well as the stresses depend only on the radial direction. As for the pressure, it can be easily shown using the radial component of the momentum equation that it varies only in the axial direction. From the axial component of the momentum equations we obtain

$$\frac{1}{r} \frac{\partial}{\partial r} (r \tau_{rz}) = \frac{dP}{dz} \quad (17)$$

which using Eq. (3) gives

$$\frac{1}{r} \frac{\partial}{\partial r} \left( r \left( \tau_{prz} + \beta \frac{dv_z}{dr} \right) \right) = \frac{dP}{dz} \quad (18)$$

Moreover, for the affine PTT constitutive model,  $\xi_s = 0$ , the normal radial and azimuthal components of the polymeric stresses vanish

$$\tau_{prr} = \tau_{p\theta\theta} = 0 \quad (19a)$$

while the following reduced equations determine the remaining two stress components

$$Y(\underline{\underline{\tau}}_p) \tau_{prz} = (1 - \beta) \frac{dv_z}{dr} \quad (19b)$$

$$Y(\underline{\underline{\tau}}_p) \tau_{pzz} = 2Wi \tau_{prz} \frac{dv_z}{dr} \quad (19c)$$

Eqs. (18), (19b) and (19c) can be solved numerically by imposing on the annular die walls ( $r = a, r = 1$ ) the no-slip condition,  $v_z = 0$ . The pressure drop,  $dP/dz$ , which appears in the above equations, is determined by requiring that the mean velocity is equal to unity, since the mean velocity at the inflow boundary,  $V$ , is used as a characteristic velocity for making the model equations dimensionless. Therefore the additional equation that arises is

$$\bar{v}_z = 2 \int_a^1 v_z r dr = 1 \quad (20)$$

### 3. Numerical implementation

In order to solve numerically the above set of equations we have chosen the mixed finite element method to discretize the velocity, pressure and stress fields, combined with an elliptic grid generation scheme for the tessellation of the deformed physical domain.

#### 3.1. Elliptic grid generation

The grid generation scheme consists of a system of quasi-elliptic partial differential equations, capable of generating a boundary fitted tessellation of the deforming domain occupied by the liquid. Here we will only present our adaptation of its essential features to the current problem. The interested reader may refer to Dimakopoulos and Tsamopoulos [18] for further details on all the important issues of the method. With this scheme the physical domain  $(r, z)$  is mapped onto a computational one  $(\eta, \xi)$ . A fixed computational mesh is generated in the latter domain while, through the mapping, the corresponding mesh in the physical domain follows its deformations. As computational domain we choose here the volume that would be occupied by the fluid if there was no swelling at all during the extrusion and the extruded material retained the same cross-section that it had inside the die. This mapping is based on the solution of the following system of quasi-elliptic partial differential equations

$$\nabla \cdot \left\{ \left( \varepsilon_1 \sqrt{\frac{r_\xi^2 + z_\xi^2}{r_\eta^2 + z_\eta^2}} + (1 - \varepsilon_1) \right) \nabla \xi \right\} = 0 \quad (21)$$

$$\nabla \cdot \nabla \eta = 0 \quad (22)$$

where the subscripts denote differentiation with respect to the indicated variable and  $\varepsilon_1$  is a parameter that controls the smoothness of the mapping relative to the degree of orthogonality of the mesh lines. This is adjusted by trial and error; here it is set to 0.1. Moreover, it should be noted that special care was taken so that the mesh lines of the computational domain are clustered near the die exit in the  $\xi$ -direction (axially) and near the die walls in the  $\eta$ -direction (radially) in order to better resolve the widely known singularity that arises there. This was performed following the ideas in Chung [30]. More details and the exact formulas that were used can be found in Karapetsas [31].

In order to solve the above system of differential equations, appropriate boundary conditions must be imposed. On the fixed boundaries, we impose the equations that define their position, and the remaining degrees of freedom are used for optimally distributing the nodes along these boundaries. In addition, along the moving interface we impose the no penetration condition:

$$\underline{n} \cdot \underline{v} = 0 \quad (23)$$

together with a condition that imposes the appropriate distribution of nodes along the free surface; see Dimakopoulos and Tsamopoulos [18]. In order to illustrate the quality of the resulting mesh produced following our method we present in Fig. 2 a blowup of the physical domain close to the die exit, restricting  $z$  to  $0.8 \leq z \leq 4.5$ , whereas  $l_1 = 1.5$  and  $l_2 = 15$ . As we can see the mesh is denser where it is needed the most, around the two triple contact points because it is well-known that a singularity arises there which requires special attention. For clarity in this figure, we show the rectangular elements generated by our mesh generation method and before appropriately splitting each rectangle into two triangles and a case with 20 and 330, radial and azimuthal elements, respectively. We should note here that the splitting of the rectangular elements should be performed so that at each lip of the annular die four triangular elements share one of their nodes. In this way the shape of

the triangular elements in that region will not be significantly distorted even for very large deformations of the extrudate permitting the calculations up to very high Weissenberg numbers.

#### 3.2. Mixed finite element method

The computational domain is tessellated using triangular elements because they conform better to the large deformations of the physical domain and can sustain larger distortions than the rectangular ones. We approximate the velocity and position vector with 6-node Lagrangian basis functions,  $\phi^i$ , and the pressure, the elastic stresses as well as the velocity gradients with 3-node Lagrangian basis functions,  $\psi^i$ .

For the momentum and mass balances we employ the finite element/Galerkin method, which after applying the divergence theorem reduces them into the following weak forms

$$\int_{\Omega} [Re \underline{v} \cdot \nabla \underline{v} \phi^i - P \nabla \phi^i + \nabla \phi^i \cdot \underline{\Sigma} + 2 \nabla \phi^i \cdot \underline{\dot{\gamma}}] d\Omega - \int_{\Gamma} [\underline{n} \cdot \underline{\sigma}] \phi^i d\Gamma = 0 \quad (24)$$

$$\int_{\Omega} \psi^i \nabla \cdot \underline{v} d\Omega = 0 \quad (25)$$

where  $d\Omega$  and  $d\Gamma$  are the differential volume and surface area, respectively. Henceforth, we will set  $Re = 0$ , because viscous forces dominate inertia in most polymeric flows. The surface integral that appears in the momentum equation is split into six parts, each one corresponding to a boundary of the physical domain and the relevant boundary condition is applied therein.

The weak form of the mesh generation equations is derived similarly by applying the divergence theorem:

$$\int_{\Omega} \left( \varepsilon_1 \sqrt{\frac{r_\xi^2 + z_\xi^2}{r_\eta^2 + z_\eta^2}} + (1 - \varepsilon_1) \right) \nabla \xi \cdot \nabla \phi^i d\Omega = 0 \quad (26)$$

$$\int_{\Omega} \nabla \eta \cdot \nabla \phi^i d\Omega = 0 \quad (27)$$

The continuous approximation of the components of the velocity gradient tensor is determined by

$$\int_{\Omega} (\underline{G} - \nabla \cdot \underline{v}) \psi^i d\Omega = 0 \quad (28)$$

Finally the constitutive equation, due to its hyperbolic character, is discretized using the SUPG method proposed by Brooks and Hughes [32]

$$\int_{\Omega} \left[ Y(\underline{\tau}_p) \underline{\Sigma} + Wi \underline{\Sigma} + 2Wi(1 - \beta) \underline{D} - 2(1 - \beta)(1 - Y(\underline{\tau}_p)) \underline{D} \right] \chi^i d\Omega = 0 \quad (29)$$

where the weighting function  $\chi^i$  is formed from the finite element basis function for the elastic stress components according to

$$\chi^i = \psi^i + \frac{h}{|\underline{v}|} \underline{v} \cdot \nabla \psi^i \quad (30)$$

where  $|\underline{v}|$  is the mean velocity and  $h$  is a characteristic length in each element. The mean velocity  $|\underline{v}|$  in an element is defined as  $|\underline{v}| = 1/3 \sum_{n=1}^3 |\underline{v}|_n$ ,  $|\underline{v}|_n$  denoting the magnitude of the velocity at the vertices of the corresponding triangular element. As a characteristic

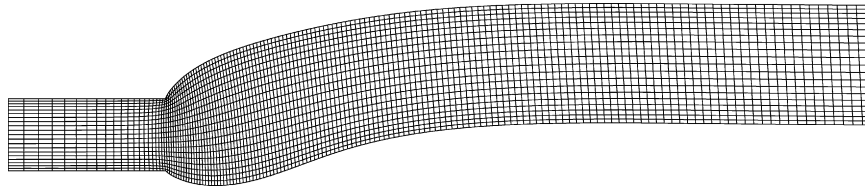


Fig. 2. Typical mesh for  $Wi=0.4$ ,  $\varepsilon=0.02$ ,  $\beta=0.111$  and  $a=0.7$ ,  $l_1=1.5$ ,  $l_2=15$ . For clarity we show rectangular elements for  $0.8 \leq z \leq 4.5$ .

length,  $h$ , we used the square root of the area of each triangular element.

Dimakopoulos and Tsamopoulos [21] have proposed a decoupled scheme for solving the momentum, stress and mesh equations which has proved very robust and fast for solving time-dependent problems. However, this scheme was not as successful in solving the steady viscoelastic annular extrusion, because convergence failed at relatively low Weissenberg numbers. Instead we solved the resulting set of algebraic equations simultaneously for all variables (velocities, pressure, stresses, node location) using the Newton–Raphson method, which permitted convergence up to high Weissenberg numbers. The entire Jacobian matrix that is generated, during each Newton iteration, is stored in compressed sparse row (CSR) format. An additional advantage of this method is that the Jacobian matrix is now available for determining the linear stability analysis of this flow. Two different methods have been used for the solution of the linearized equations. The first one uses a Krylov iteration method, BI-CGSTAB [33] with an incomplete LU preconditioning, while the second one resorts to Gaussian elimination using PARDISO, a robust direct sparse matrix solver, Schenk and Gärtner [34,35]. Although the solution of one step of the Newton–Raphson method was faster with BI-CGSTAB than with PARDISO, the performance of the latter was enhanced significantly by the use of the modified Newton–Raphson method, which does not update the Jacobian matrix and its LU decomposition after each iteration, but only after a criterion of decreased convergence rate is exceeded. With this technique PARDISO needed less time than BI-CGSTAB to perform a continuation in the Weissenberg number. The iterations of the Newton–Raphson method are terminated using a tolerance for the absolute error of the residual vector, which is set at  $10^{-9}$ . The code was written in Fortran 90 and was run on a workstation with dual Dual Core Xeon CPU at 2.8 GHz in the laboratory of computational fluid dynamics. Each calculation typically required 1–2 days to complete.

## 4. Results and discussion

### 4.1. Fully developed flow inside an annular die

As mentioned earlier, at the inflow boundary, the velocity field as well as the elastic stresses must be imposed. For that reason we have to solve numerically the one-dimensional momentum and constitutive equations for the fully developed viscoelastic annular flow. It would be useful to present these results separately, since laminar annular flows of non-Newtonian fluids are frequently encountered in industry, such examples being flow inside an annular extruder, flow inside an annular heat exchanger and flow between the drilling shaft and the surrounding soil. A nice presentation of the earlier works in this area has been given by Pinho and Oliveira [36]. To our surprise we found out that when it comes to viscoelastic annular flows very few theoretical/numerical works exist in the literature. Pinho and Oliveira [36] published recently an analytical solution for a viscoelastic fluid using the linear PTT model, assuming that the intermolecular slip parameter,  $\xi_s$ , as well as the viscosity ratio,  $\beta$ , are both equal to zero. We will present here results for the expo-

nenial PTT model allowing for the solvent viscosity ratio,  $\beta$ , to have nonzero values while retaining  $\xi_s = 0$ . Primarily because of the exponential function in the constitutive equation, this form of the PTT model does not admit an analytical solution.

Fig. 3 shows the velocity profiles for various  $Wi$  numbers and for  $\varepsilon=0.02$ ,  $\beta=0.111$  and  $\alpha=0.7$ . Although the profiles may generally seem to be symmetric with respect to the mid point of the annular opening, closer observation reveals that they are not symmetric and they should not be in an annular geometry. As expected for low elasticity ( $Wi=0.1$ ) the velocity profile resembles the one from the Newtonian case, while as  $Wi$  increases the profile changes significantly becoming more flattened indicating the effect of shear thinning. Such an effect is not present in purely elastic fluid models ( $\varepsilon=0$ ), e.g. the Oldroyd-B model, but it is present in a PTT fluid. We observe though that this variation is not monotonic. For example, the maximum value of the axial velocity decreases as  $Wi$  increases up to  $Wi=2$ , whereas it increases when  $Wi$  increases further. This is in contrast with the solution for the velocity profile provided by Pinho and Oliveira [36] for  $\beta=0$  where a monotonic variation of the max  $v_z$  was observed. We believe that this non-monotonic behavior is caused by the presence of the solvent viscosity in the model. Another indication that this is the case is provided by Cruz et al. [37] who developed an analytical solution for the flow inside a cylindrical pipe considering a linear PTT fluid with a Newtonian solvent contribution ( $\beta \neq 0$ ). Although they studied thoroughly the effect of the ratio of the solvent viscosity over the total viscosity,  $\beta$ , they did not report results showing the effect of the Weissenberg number. From their analytical solution however, it can be easily shown that as  $Wi$  increases the same non-monotonic variation of the velocity profile arises.

The overall variation of the velocity profile is primarily caused by the shear-thinning nature of the PTT fluid model, through the parameter  $\varepsilon$ . Fig. 4 shows the dependence of the ratio of the local shear viscosity over the zero shear viscosity on the radial position for various  $Wi$  values and for the same other parameters as

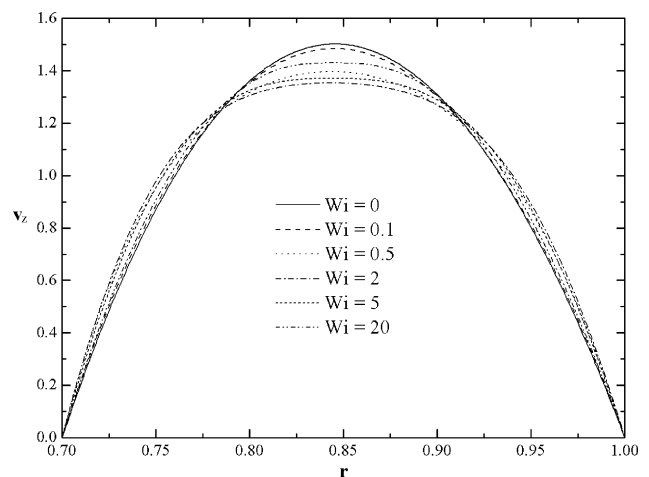


Fig. 3. Velocity profiles for various  $Wi$  and for  $\varepsilon=0.02$ ,  $\beta=0.111$ ,  $\alpha=0.7$ .

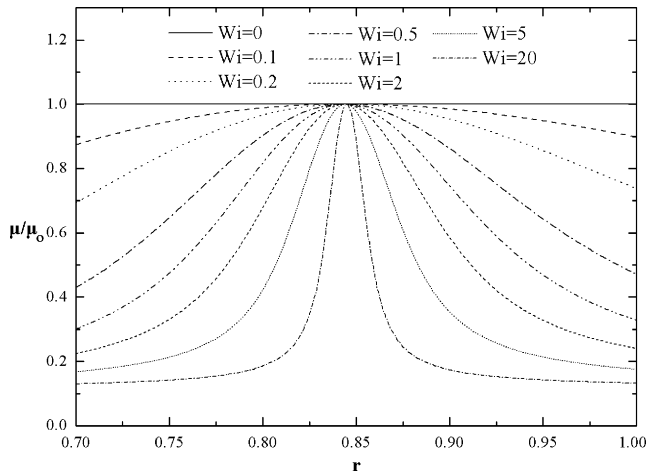


Fig. 4. Shear viscosity for various  $Wi$  and for  $\varepsilon=0.02$ ,  $\beta=0.111$ ,  $a=0.7$ .

in Fig. 3. For all values of  $Wi$  the shear viscosity of a PTT fluid approaches its upper limiting value and  $\mu/\mu_0 = 1$  for vanishing shear rate at a particular point of the annular gap. For low elasticity ( $Wi=0.1$ ) this ratio of shear viscosities remains almost unity everywhere except for a small region near the walls where the shear rate is higher causing shear thinning in the material. As  $Wi$  increases the viscosity decreases even more, because the exponential term inducing shear thinning in the PTT model increases both with  $\varepsilon$  and  $\lambda$  (or  $Wi$ ); see also the analytical expression given by Pinho and Oliveira [36] (their Eq. (11)). For  $Wi \leq 2$  the viscosity changes gradually all over the flow domain. However for higher  $Wi$  numbers the flow domain seems to be divided in two regions. A region near the annular die walls, where the viscosity is almost uniform and has very low values due to the increased shear-thinning, and one in the middle where the shear viscosity increases abruptly because of the low shear rate in that area. This dual nature of the shear viscosity predicted by this PTT model resembles the one imposed by the so-called bi-viscosity models. We also observe that for high elasticity ( $Wi=20$ ) the shear viscosity near the die walls has almost reached its asymptote to the Newtonian solvent viscosity because of the very high shear rate that arises there. The existence of the two distinct regions one of high and variable viscosity and the other with low and almost constant viscosity that appear in the higher  $Wi$  number profiles of shear viscosity directly corresponds to the velocity profiles that are nearly flat around the middle of the annular opening.

The effect of elasticity on the polymeric part of the shear stress,  $\tau_{prz}$ , and the normal stress,  $\tau_{pzz}$ , is given in Fig. 5a where we show their variation across the annular gap. The magnitude of the shear stress decreases monotonically with  $Wi$  in contrast to the magnitude of the normal stress whose variation is nonmonotonic. Pinho and Oliveira [36] noted that, when  $\beta=0$ , if the stresses are scaled with the inner wall shear stress,  $\tau_w$ , then all the different curves for the shear stress collapse onto a single curve while the variation of the normal stress becomes monotonic as  $Wi$  increases. When a Newtonian solvent contribution is present ( $\beta=0.111$ ), as it is shown in Fig. 5b, the curves for the shear stress do not collapse on a single curve while the variation of the normal stresses still becomes monotonic. Moreover we observe that the axial stresses become more and more significant compared to the shear stresses as the  $Wi$  number increases due to elasticity.

It would be interesting to study the effect of the elongation parameter,  $\varepsilon$ , which introduces in the PTT model the effect of shear and elongational thinning. Fig. 6 shows the velocity profiles for

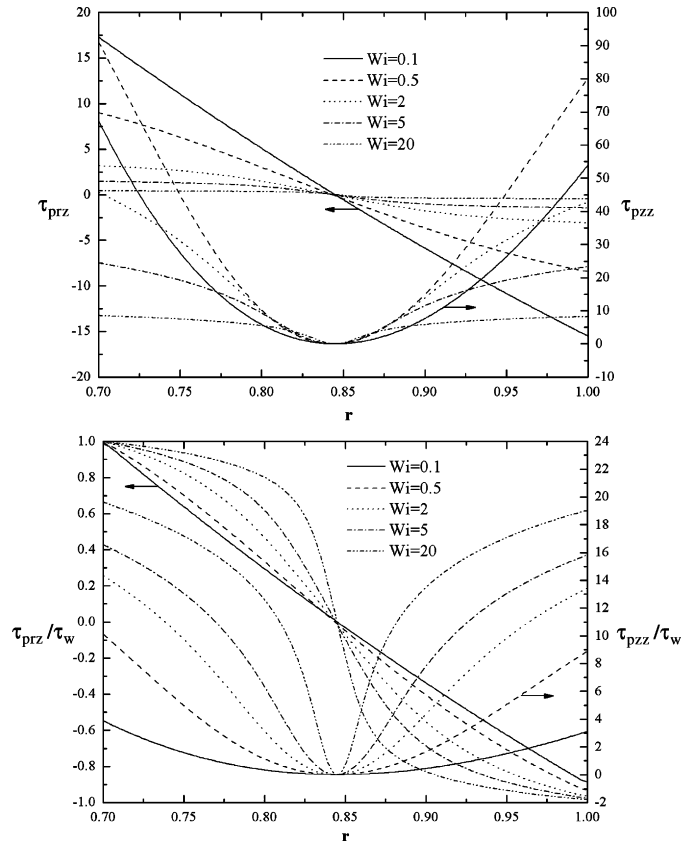


Fig. 5. (a) Stress profiles for various  $Wi$  and for  $\varepsilon=0.02$ ,  $\beta=0.111$ ,  $a=0.7$  and (b) stress profiles scaled with the inner wall shear stress for various  $Wi$  and for  $\varepsilon=0.02$ ,  $\beta=0.111$ ,  $a=0.7$ .

$Wi=1$ ,  $\beta=0.111$  and  $a=0.7$  for various values of  $\varepsilon$ . For  $\varepsilon=0$  the velocity profile is the same with a Newtonian fluid while the solution is independent of  $Wi$ , since the solution for an Oldroyd-B fluid is the same for all  $Wi$  numbers. Moreover, we observe that for high values of  $\varepsilon$ , the variation of the velocity profile is again nonmonotonic. From Fig. 7, which shows the variation of the shear viscosity along the radial direction for the same parameters as in Fig. 6, we deduce that the change in the monotonicity of the velocity profile occurs

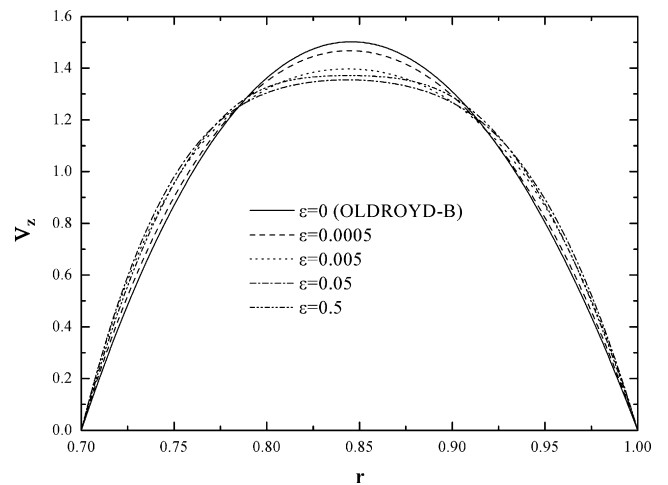


Fig. 6. Dependence of the velocity profile on the elongation parameter  $\varepsilon$  for  $Wi=1$ ,  $\beta=0.111$ ,  $a=0.7$ .

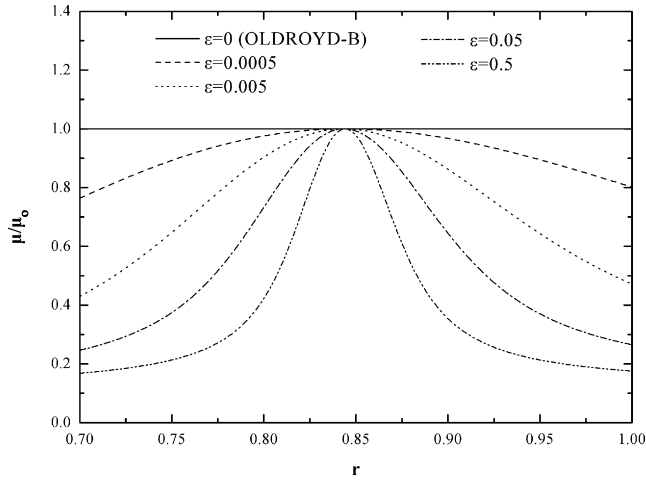


Fig. 7. Dependence of the shear viscosity on the elongation parameter  $\varepsilon$  for  $Wi=1$ ,  $\beta=0.111$ ,  $a=0.7$ .

around the value of  $\varepsilon$  for which the same qualitative change in the shear viscosity variation arises as in Fig. 4, where the dependence of the shear viscosity on  $Wi$  was presented. Indeed, whereas for low values of  $\varepsilon$  the shear viscosity changes gradually along the radial direction, for  $\varepsilon=0.5$  the shear viscosity exhibits low and almost constant values for a wide region near the annular die walls, while it rises abruptly around the middle. For this value of  $\varepsilon$  the velocity profile is closest to becoming uniform for a fairly wide area around the middle of the gap.

The dependence of shear and normal stresses on the radial distance is shown in Fig. 8. Once again, the magnitude of the shear stress,  $\tau_{prz}$ , decreases monotonically with  $\varepsilon$  due to the increased shear thinning. As for the normal stress,  $\tau_{pzz}$ , it takes very high values near the die walls for  $\varepsilon=0$  since the Oldroyd-B model predicts infinite elongational viscosity at higher shear rates. However, as  $\varepsilon$  increases the elongational viscosity takes finite values which decrease with  $\varepsilon$  and, consequently, the normal stress,  $\tau_{pzz}$ , decreases.

Fig. 9 presents the dependence of the velocity profile on the solvent viscosity ratio for  $Wi=1$ ,  $\varepsilon=0.02$  and  $a=0.7$ . As expected for high solvent fraction,  $\beta=0.9$ , the profile resembles the one of a Newtonian fluid. As  $\beta$  decreases and the fluid becomes more elastic the velocity profile becomes flatter. This happens because as can be seen in Fig. 10 the shear viscosity compared to the zero shear rate

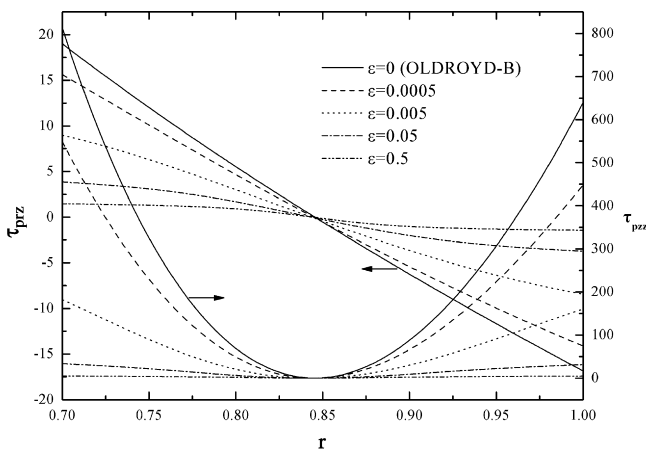


Fig. 8. Dependence of the stress profile on the elongation parameter  $\varepsilon$  for  $Wi=1$ ,  $\beta=0.111$ ,  $a=0.7$ .

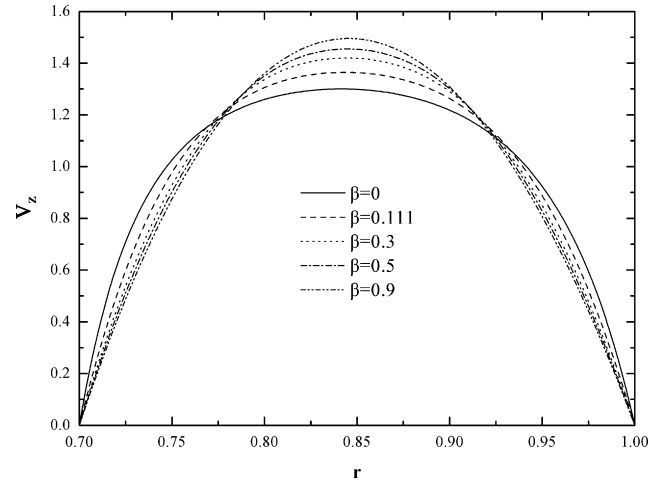


Fig. 9. Effect of the solvent viscosity ratio on the velocity profile for  $Wi=1$ ,  $\varepsilon=0.02$ ,  $a=0.7$ .

viscosity for  $\beta=0.9$  is very close to unity, whereas as  $\beta$  decreases the shear thinning of the viscoelastic fluid becomes more significant. For the particular choice of  $Wi$  and  $\varepsilon$  in Figs. 9 and 10 the viscosity profile never becomes flat near the wall and correspondingly the velocity profile never becomes nearly flat around the middle of the gap, irrespective of the value of  $\beta$ . The variations for both the shear and normal stresses with  $\beta$ , at fixed  $Wi$ , are qualitatively similar to those in Fig. 8 and will not be given here; Karapetsas [31].

It is interesting to see the effect of the solvent viscosity ratio on the Fanning friction factor, which is the dimensionless pressure gradient driving the flow and, hence, an important engineering parameter. The friction factor for an annular die is defined as

$$f \equiv -\frac{dP}{dz} \frac{2(1-a)^2}{Re} \quad (31)$$

In order to study how the viscoelastic results differ from the Newtonian solution we show in Fig. 11 the dependence of the ratio of  $fRe$  to the corresponding Newtonian value,  $(fRe)_N$ , on the group  $\varepsilon^{1/2}Wi_\delta$  for various values of the solvent viscosity ratio. With  $Wi_\delta$  we denote the Weissenberg based on the annular gap,  $\delta=R_o-R_i$ , and thus  $Wi_\delta = \lambda U/\delta = Wi/(1-\alpha)$ . Pinho and Oliveira [36] noted that there is no influence of the radius ratio,  $a$ , on the variation of the friction factor with elasticity, when it is measured by  $\varepsilon^{1/2}Wi_\delta$ , which

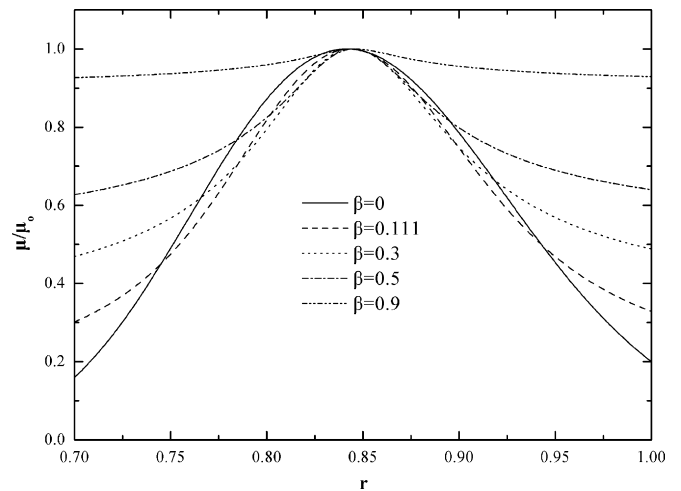


Fig. 10. Effect of the solvent viscosity ratio on the shear viscosity for  $Wi=1$ ,  $\varepsilon=0.02$ ,  $a=0.7$ .

**Table 1**  
Properties of typical finite element meshes used in this paper ( $a=0.9$ ,  $l_1=1$ ,  $l_2=50$ )

Mesh	Number of 1D radial elements	Number of 1D axial elements	Number of triangular elements	Number of unknowns	$\Delta r_{\min}$	$\Delta z_{\min}$
M1	10	165	3,300	46,064	0.010	0.022
M2	15	250	7,500	102,284	0.007	0.013
M3	20	330	13,200	177,914	0.005	0.010
M4	25	415	20,750	277,684	0.004	0.007
M5	30	500	30,000	399,554	0.003	0.006

combines fluid elasticity and extensibility in a way that is most appropriate for a PTT fluid; see also Oliveira and Pinho [38]. Then all the curves of the friction factor collapse onto a master curve. The same holds even in our case where a Newtonian solvent contribution is present and each curve of  $fRe/(fRe)_N$  for a given  $\beta$  is also a master curve. The friction factor ratio decreases very quickly for low values of  $\varepsilon^{1/2}Wi_\delta$ , due to shear thinning, while it gradually levels off at higher values of  $\varepsilon^{1/2}Wi_\delta$ . Furthermore, as  $\beta$  increases the friction factor departs less from the Newtonian case, as expected. It is noteworthy that in these calculations  $Wi$  and even more so  $Wi_\delta$  assume very large values, without causing any numerical problems.

#### 4.2. Annular die swell

In order to describe the swelling of the annular extrudate in the numerical simulations that follow one can use three parameters, only two of which are independent: the outer radius swell,  $Sw_o$ , the inner radius swell,  $Sw_i$  and the thickness swell,  $Sw$ , which are defined as

$$Sw_o = \frac{H_o}{R_o} \quad (32a)$$

$$Sw_i = \frac{H_i}{R_i} \quad (32b)$$

$$Sw = \frac{H_o - H_i}{R_o - R_i} \quad (32c)$$

Moreover, the total pressure drop in the system,  $\Delta P$ , was also used to evaluate the exit pressure losses, which is an important design parameter, defined as

$$Ex = \frac{\Delta P - \Delta P_o}{2\tau_w} \quad (33)$$

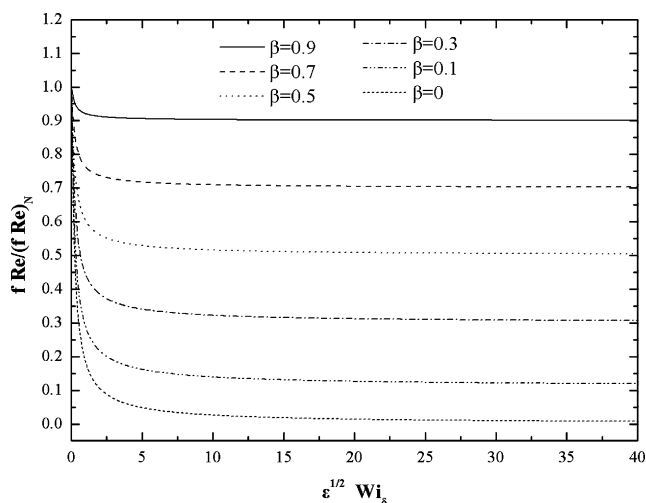


**Fig. 11.** Ratio of the viscoelastic to the Newtonian friction factor as a function of  $\varepsilon^{1/2}Wi_\delta$  for various solvent viscosity ratios.

where  $\Delta P_o$  is the pressure drop for fully developed flow in a straight annulus of the same length and radius ratio as the die, and  $\tau_w$  the corresponding shear stress at the inner die wall.

#### 4.2.1. Code validation

First, we performed several tests in order to check the convergence of the numerical procedure and the overall solution accuracy. Some useful data concerning the meshes which were used in this study are presented in Table 1.

The convergence with mesh refinement of the final outer and inner radius and thickness swell ratios of the annular extrudate for  $\varepsilon=0.02$ ,  $\beta=0.3$ ,  $a=0.9$ ,  $l_1=1$ ,  $l_2=50$  and for two different  $Wi$  numbers is presented in Table 2. Evidently, the calculated swelling ratios converge with mesh refinement. We should note also that the convergence rate with mesh refinement is influenced mainly by the value of  $\varepsilon$ . In this Table data are reported for quite low values of  $\varepsilon$ . Increasing this parameter, typically improves the convergence rate, since it decreases the elongational viscosity and increases shear thinning (see also Fig. 8) reducing the stress gradients. On the other hand, it should be expected that for low values of  $\varepsilon$  steeper stress gradients will arise, especially near geometric singularities, making necessary local refinement of the mesh around these regions in order to adequately resolve the stresses. Hence, special care was taken so that the size of the elements around the triple contact points is kept roughly constant and smaller than in other parts of the domain; see also Fig. 2. In all cases to be presented subsequently a mesh was used with node distribution the same as that in the M3 mesh. Depending on the gap opening the density in the  $r$ -direction could vary slightly, but not the number of nodes in this direction.

To quantify the error and its dependence on the mesh we prepared Fig. 12. The rate of convergence with mesh refinement is assessed by computing the Euclidean norm of the differences of the values at the die exit ( $z=l_1$ ) obtained with any mesh to those obtained by the finest mesh (M5) for the same variables. This is a very strict test as the norms are not “diluted” with parts of the solution which is easily and fully converged, i.e. away from the singular points, but are affected by the presence of the two singularities that arise at the two die lips of the annular die. For the computation of the norms the values of all variables at meshes other than the

**Table 2**  
Calculated outer, inner radius and thickness of the annular extrudate for  $\varepsilon=0.02$ ,  $\beta=0.3$ ,  $a=0.9$ ,  $l_1=1$ ,  $l_2=50$

Mesh	$Sw_o$	$Sw_i$	$Sw$
<i>Wi</i> = 0.1			
M1	1.08707	1.02860	1.61326
M2	1.10038	1.03732	1.66787
M3	1.10563	1.04146	1.68309
M4	1.11403	1.04692	1.71801
M5	1.11661	1.04905	1.72459
<i>Wi</i> = 1.0			
M1	1.46981	1.45967	1.56098
M2	1.52798	1.51312	1.66172
M3	1.56497	1.54956	1.70355
M4	1.58631	1.57041	1.72944
M5	1.59793	1.58236	1.73798

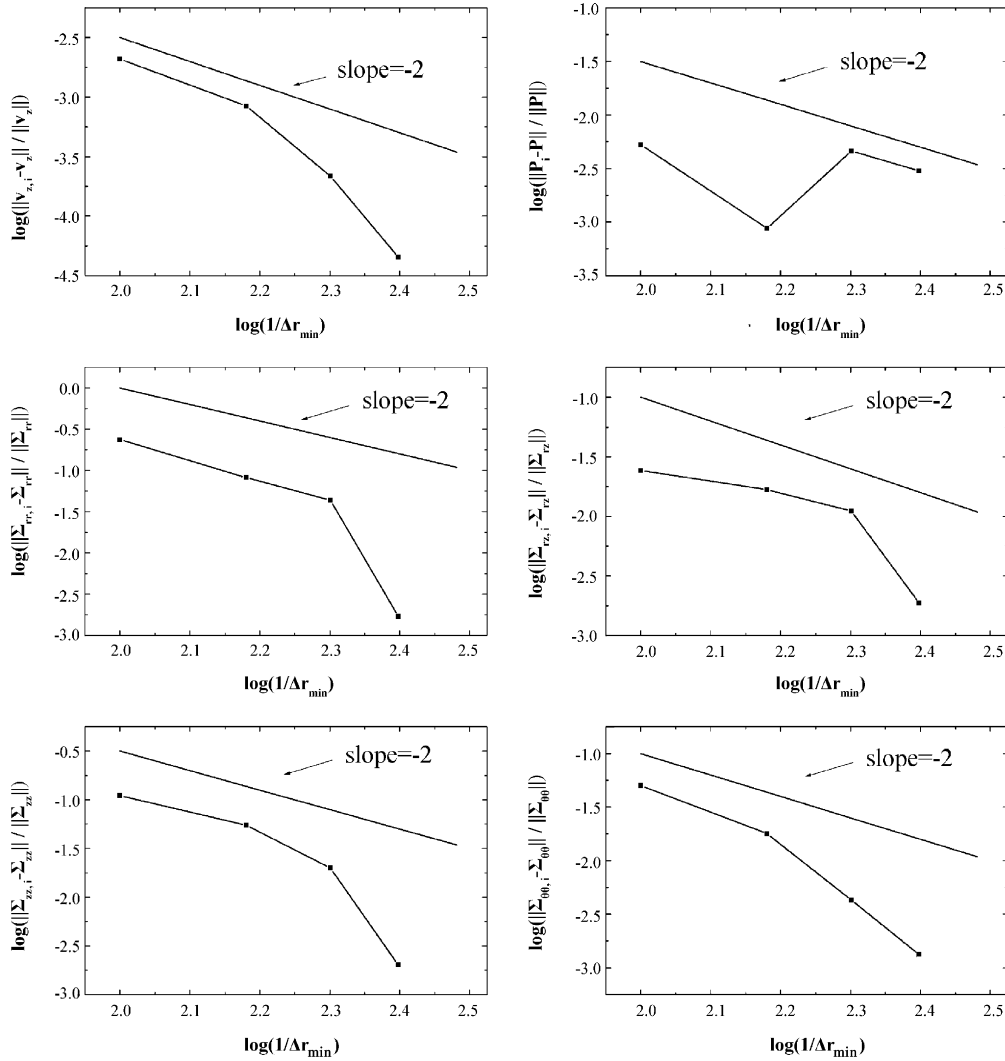


**Fig. 12.** The relative error of the axial velocity, the pressure and the stresses at the die exit ( $z=l_1$ ) for  $Wi=1$ ,  $\varepsilon=0.02$ ,  $\beta=0.3$ ,  $\alpha=0.9$ ,  $l_1=1$ ,  $l_2=50$  and various meshes. As a reference value the solution with the mesh M5 is used, while the vectors  $v_{z,i}$ ,  $P_i$ ,  $\Sigma_{rr,i}$ ,  $\Sigma_{rz,i}$ ,  $\Sigma_{zz,i}$ ,  $\Sigma_{\theta\theta,i}$  are calculated using the meshes M1, M2, M3 and M4.

coarsest one were interpolated at the locations corresponding to the coarsest mesh. Clearly for the axial velocity and the stresses the relative error decreases more than quadratically with mesh refinement. As for the pressure we observe that its relative error does not decrease monotonically with mesh for the coarsest meshes. However even for the coarsest mesh the relative error of the pressure is smaller than that of the stresses.

Another important factor is the location of the inflow and outflow boundaries where we consider the flow to be fully developed and impose the respective boundary conditions. Their position should be chosen so that it has no effect on any of the problem variables. Indeed Table 3 for  $Wi=1$ ,  $\varepsilon=0.02$ ,  $\beta=0.111$ ,  $\alpha=0.9$  shows that the swelling ratios are affected only in the fourth significant digit, while increasing the location of the two exterior boundaries

**Table 3**  
Dependence of the calculated outer and inner final extrudate radius on the distance of the inflow and outflow boundaries from the annular die exit for  $Wi=1$ ,  $\varepsilon=0.02$ ,  $\beta=0.111$  and  $\alpha=0.9$

$l_1$	$l_2$	$Sw_o$	$Sw_i$	$Sw$
1	25	1.55550	1.54792	1.62372
2	50	1.55821	1.55134	1.62003

by a factor of two. In all cases to be presented in the following, the length inside the annular die has been set at 5–10 times the die width,  $\delta$ , whereas the length of the extrudate outside the die has been increased until convergence.

Finally we compared our results with the ones given by Crochet and Keunings [4] for a Newtonian or a UCM fluid with  $\varepsilon=0$ ,  $\beta=0$ , and  $Wi=0.0276$  which corresponds to  $De=0.7$  according to their definition and is the largest value of this parameter used in that paper. The die size and the extend of the computational domain are determined from  $a=0.75$ ,  $l_1=1.5$ ,  $l_2=15$ . Table 4 demonstrates that the agreement between the two sets of data is very satisfactory.

**Table 4**  
Comparison of the swelling for an annular die as given by Crochet and Keunings [4] and predicted by the present analysis for either a Newtonian or a UCM fluid ( $Wi=0.0276$ ,  $\varepsilon=0$ ,  $\beta=0$ ,  $\alpha=0.75$ ,  $l_1=1.5$ ,  $l_2=15$ )

	$Sw_o$	$Sw_i$	$Sw$	Ex
Newtonian				
Present analysis	1.057	1.018	1.173	0.16
Crochet and Keunings [4]	1.055	1.016	1.170	0.14
$Wi=0.0276$				
Present analysis	1.060	1.022	1.176	0.27
Crochet and Keunings [4]	1.059	1.022	1.174	0.27

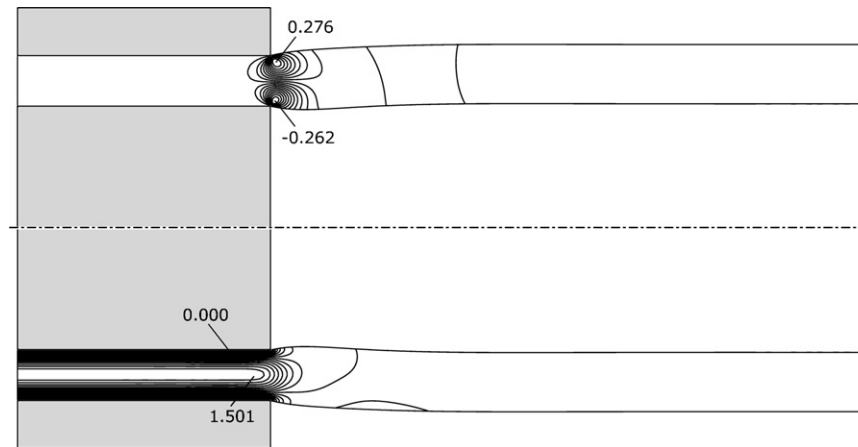


Fig. 13. Contour plots of radial, upper half, and axial velocity, lower half, for a Newtonian fluid and for  $a=0.7$ ,  $l_1=1.5$ ,  $l_2=25$ .

#### 4.2.2. Effect of viscoelasticity

To set the stage for the discussion that follows, it is useful to examine first the extrusion of a Newtonian fluid ( $Wi=0$ ) from an annular die. Fig. 13 illustrates the flow field for an annular die with radius ratio  $a=0.7$  and  $l_1=1.5$ ,  $l_2=25$ . In addition to the shape of the extrudate, this figure presents the contour plots of the radial and axial velocity, on the upper and lower half, respectively. The total number of contour lines in each part of this and all subsequent similar plots is 20, unless it is denoted otherwise. The radial velocity is zero almost everywhere except for a region around the die exit, where the velocity field is rearranging from the fully developed shear flow inside the die to the shear free flow outside it. The radial velocity has its maximum value (positive) near the outer free surface, while its minimum value (negative) is near the inner one, since, even for a Newtonian fluid, the extrudate swells slightly in both radial directions. Moreover, far from the die where the flow becomes again fully developed, the radial velocity tends to zero. As for the axial velocity, it has the well-known from standard textbooks profile inside the die which, as the fluid approaches and passes through the exit of the die, gradually turns into a plug flow profile. Its maximum retains the value and the location it had for fully developed flow at  $z=0$  almost all the way to the die exit.

Changing the rheological properties of the fluid should affect qualitatively certain characteristics of the flow. Fig. 14 illustrates the annular extrusion for a viscoelastic fluid with  $Wi=3$  and for  $\varepsilon=0.02$ ,  $\beta=0.3$  while the same geometric parameters are used as in the previous Newtonian case. It is obvious that the shapes of the calculated free surfaces have changed significantly. The normal stresses, which are present due to the elasticity of the material, cause much larger swelling in the extrudate than in the Newtonian case. Fig. 14a depicts contour lines of  $v_r$  and  $v_z$  on the upper and lower half of the figure, respectively. The values of the radial velocity outside the die have increased in comparison to those for a Newtonian fluid; they have almost doubled, reflecting the increased swelling of the extrudate. As for the axial velocity, while it has changed a little around the die exit, it remains qualitatively the same. The variation of the pressure field is shown on the upper half of Fig. 14b. Inside the die the pressure varies almost linearly in the axial direction, the main flow direction, up to almost the edge of the die where, as it is expected, the flow becomes two-dimensional. On the lower half of Fig. 14b, the variation of the second invariant of the rate of strain is depicted. It takes nonzero values inside the die where the flow is dominated by shear, but very small values outside the die where the flow is shear-free. Its maximum value arises at the inner die lip where, as already mentioned, a singularity in the pressure and

stress fields exists. Contour lines of  $\tau_{prr}$  and  $\tau_{prz}$ , upper and lower half of Fig. 14c, respectively, show that these stress components vary mostly around the two triple contact points and their magnitude decreases very rapidly away from them. Finally in Fig. 14d contour lines of  $\tau_{pzz}$  (upper half) and  $\tau_{p\theta\theta}$  (lower half) are given. The axial normal stress varies mainly inside the die and takes its maximum value at the inner die lip, while outside the die it decreases rapidly except for the surface of the extrudate, where it takes longer to become zero. On the contrary, the azimuthal normal stress,  $\tau_{p\theta\theta}$ , varies mainly outside the die where the swelling of the fluid takes place. By focusing on the upper lip of the die exit we can examine closer the polymeric stresses,  $\tau_{prz}$  and  $\tau_{pzz}$ . This is shown in Fig. 15, which gives 20 contour lines for each stress component only in the region  $r \geq 0.81$  and  $1 \leq z \leq 2.1$ . The smoothness of the contours (without any special post-processing of the raw data) testifies the high quality of the obtained results, still with the M3 mesh given in Table 1. Moreover, the closeness of the stress contours not only at the corner itself but also at the nearby free surface of the extrudate indicates that the corner singularity may help in generating boundary layers in stress further downstream.

To examine the effect of the Weissenberg number on the stress tensor, we have plotted in Fig. 16 the contour lines of  $\tau_{pzz}$  (upper half) and  $\tau_{p\theta\theta}$  (lower half) for  $Wi=1$  while keeping the rest of the parameters the same as in Fig. 14. We observe that by decreasing  $Wi$  the values of the stresses increase, while qualitatively their variation remains the same. This seemingly unexpected trend, in fact, agrees with the results in Fig. 5a, where it was observed that inside the die and for fully developed flow the values of  $\tau_{prz}$  and  $\tau_{pzz}$  increase rapidly for  $Wi$  up to 0.5, while from  $Wi=2$  and above they decrease, because the increased  $Wi$  increases not only the elasticity level but also the shear thinning in the material.

Fig. 17 shows the dependence of the shape of the two free surfaces on the elasticity of the fluid for  $\varepsilon=0.02$ ,  $\beta=0.3$ ,  $a=0.9$ ,  $l_1=1$ ,  $l_2=30$ . Clearly, the swelling increases significantly with  $Wi$ , and for  $Wi=10$  the final outer radius of the extrudate has increased by more than 100%. In agreement with the discussion related to Fig. 16, the swelling increases faster for the lower values of  $Wi$ , whereas for larger elasticity values, shear thinning increases as well, which decreases the normal stresses and, hence, the extrudate swelling decelerates. Moreover, an interesting observation is that for high values of  $Wi$  the free surfaces are not a monotonic function of  $z$ . The axial position where the maximum is attained moves downstream as  $Wi$  increases. For  $Wi=1$  the maximum for the outer free surface is at  $z=2.201$ , while for  $Wi=10$  it is at  $z=2.269$ . In the absence of surface tension from our model, this is a clear demonstration of fluid

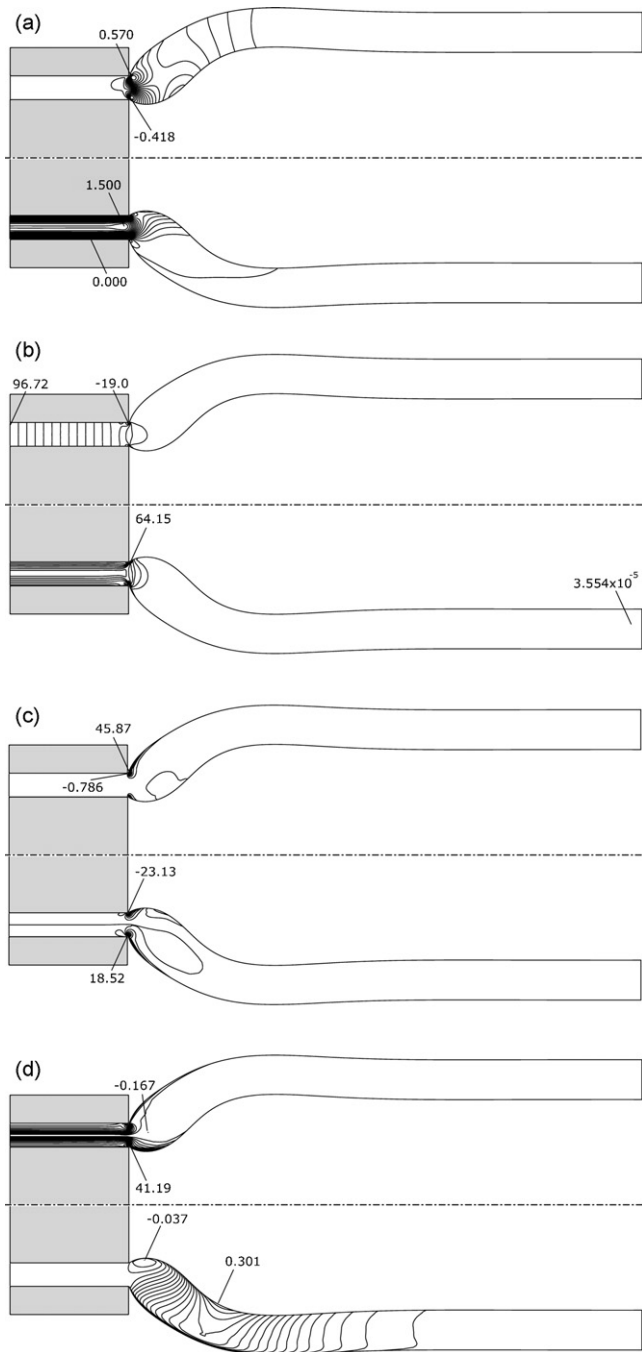


**Fig. 14.** Contour plots of (a)  $v_r, v_z$ , (b)  $P, \dot{\gamma}$ , (c)  $\tau_{prz}, \tau_{prz}$ , (d)  $\tau_{pzz}, \tau_{p\theta\theta}$  on the upper and lower half, respectively for  $Wi=3, \epsilon=0.02, \beta=0.3, a=0.7, l_1=1.5, l_2=25$ . (For clarity we show the region  $0 \leq z \leq 8$ ).

elasticity which forces the material to rebound towards the axis of symmetry from its previous highest radial position. It is noteworthy that calculations could be performed for even higher values of  $Wi$  without any numerical difficulties.

4.2.3. Effect of solvent viscosity ratio

The ratio of the solvent viscosity to the total fluid viscosity,  $\beta$ , is an important parameter since it affects significantly the shear viscosity at high shear rates (see Fig. 10). Fig. 18 depicts contour lines of  $\tau_{prz}$  (upper half) and  $\tau_{p\theta\theta}$  (lower half) for  $Wi=4, \epsilon=0.02, \beta=0.9, a=0.8, l_1=1, l_2=50$ . For this large value of the solvent viscosity ratio, the distance that is needed in order for the flow to become

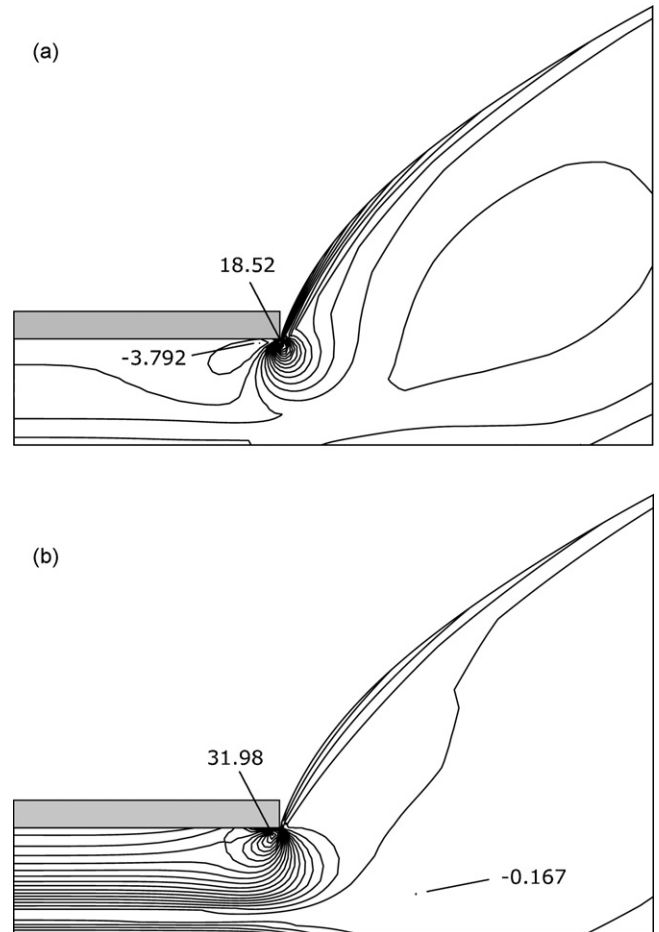


**Fig. 15.** Contour plots of (a)  $\tau_{prz}$  and (b)  $\tau_{pzz}$  around and very close to the outer wall of the die exit (the region is confined by  $r \geq 0.81$  and  $1 \leq z \leq 2.1$ ) for  $Wi=3, \epsilon=0.02, \beta=0.3, a=0.7, l_1=1.5, l_2=25$ .

fully developed outside the die is much larger. Moreover, here the extrudate swelling is not as large, although the Weissenberg number is quite large. The contour lines of the radial normal stress have changed qualitatively varying in a larger region outside the die in contrast to Fig. 14c where they varied mainly around the two triple contact points. In addition its maximum values have decreased considerably. As for the azimuthal normal stress, it has relatively small values as should be expected given the decreased swelling of the material.

Fig. 19 illustrates the dependence of the extrudate shapes for a fixed  $Wi$  number ( $Wi=1$ ) and for various values of  $\beta$ . The rest of the parameters are  $\epsilon=0.05, a=0.9, l_1=1, l_2=50$ . For high values of  $\beta$  the swelling is insignificant, because the large solvent content makes the fluid behave like a Newtonian one. Nevertheless, as  $\beta$  decreases the swelling increases up to about 40% and exhibits a nonmonotonic behavior for the two lower values of  $\beta$ . This probably occurs because, as  $\beta$  decreases, elasticity becomes more and more important resulting in larger and larger swelling ratios. However, at the same time shear thinning also becomes important, since lower values of  $\beta$  result in a lower limit for the shear viscosity of the fluid which is proportional to the solvent viscosity ratio. Therefore, the change in the monotonicity of the swelling is probably caused by the interplay between material elasticity and shear thinning. The apparent maximization in extrudate swelling at,  $\beta=0.3$  is the reason that in Fig. 17 we chose that value for  $\beta$ .

It would be interesting to examine the effect of  $\beta$  on the two different swelling ratios,  $Sw_o$  and  $Sw$ . Their dependence on the

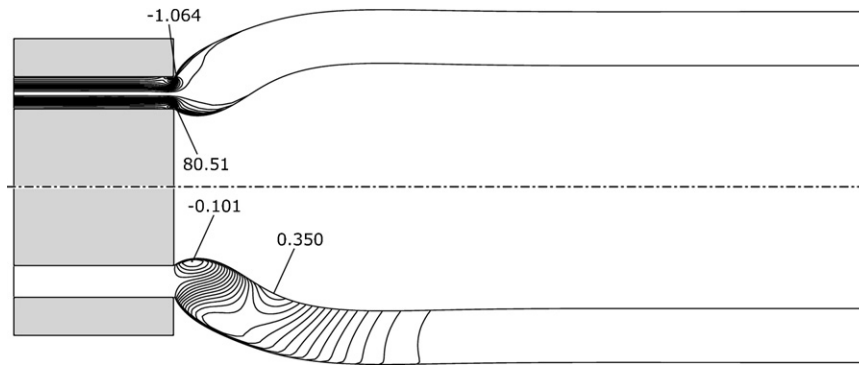


Fig. 16. Contour plots of  $\tau_{pzz}$ ,  $\tau_{p00}$  on the upper and lower half, respectively for  $Wi=1$ ,  $\varepsilon=0.02$ ,  $\beta=0.3$ ,  $a=0.7$ ,  $l_1=1.5$ ,  $l_2=25$ . (For clarity we show the region  $0 \leq z \leq 8$ ).

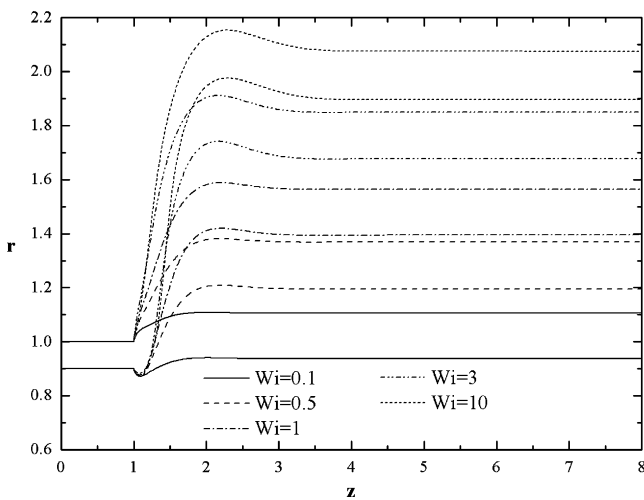


Fig. 17. Shapes of the calculated free surfaces of the annular extrudate for  $\varepsilon=0.02$ ,  $\beta=0.3$ ,  $a=0.9$ ,  $l_1=1$ ,  $l_2=30$  and various  $Wi$  numbers.

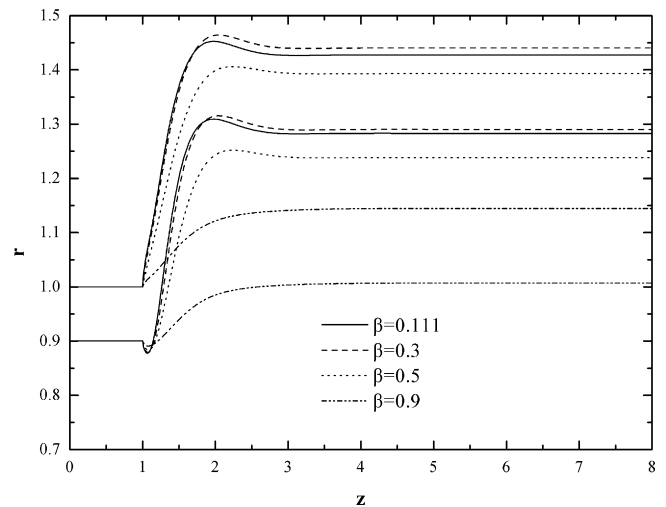


Fig. 19. Shape of the calculated free surfaces of the annular extrudate for  $Wi=1$ ,  $\varepsilon=0.05$ ,  $a=0.9$ ,  $l_1=1$ ,  $l_2=50$  and various  $\beta$ .

Weissenberg number for various  $\beta$  is depicted in Fig. 20, while the rest of the parameters are kept constant. The simulations for this case were terminated at  $Wi=20$ , since after that value the swelling of the fluid did not change significantly. The figure shows that the swelling ratio of the outer radius,  $Sw_o$ , increases as  $\beta$  decreases except for the region of  $0.7 \leq Wi \leq 3$ , where a change of monotonicity takes place for the two lower values of  $\beta$ . The variation of the inner swelling ratio is qualitatively the same and is not presented here for conciseness. An interesting observation in Fig. 20b is that the swelling ratio of the thickness for a fixed value of  $\beta$  is a complex and nonmonotonic function of  $Wi$ . Moreover, for low  $Wi$ , the smaller the solvent viscosity ratio the smaller the thickness swelling ratio,

whereas for larger  $Wi$  the thickness swelling ratio is a nonmonotonic function of  $\beta$ . The monotonicity seems to be recovered though for even higher values of  $Wi$ .

An important parameter for the industrial processes is the pressure drop and, hence, in Fig. 21 we give the dependence of the exit pressure losses,  $Ex$ , on the  $Wi$  number for various values of  $\beta$ , while keeping the rest of the parameters the same. The pressure drop initially increases with  $Wi$  while for larger values, where the effect of fluid elasticity has saturated, it decreases significantly because the effect of shear thinning has now taken over. Furthermore, the maximum value of  $Ex$  in each curve decreases as  $\beta$  increases, since then the fluid tends to the Newtonian limit.

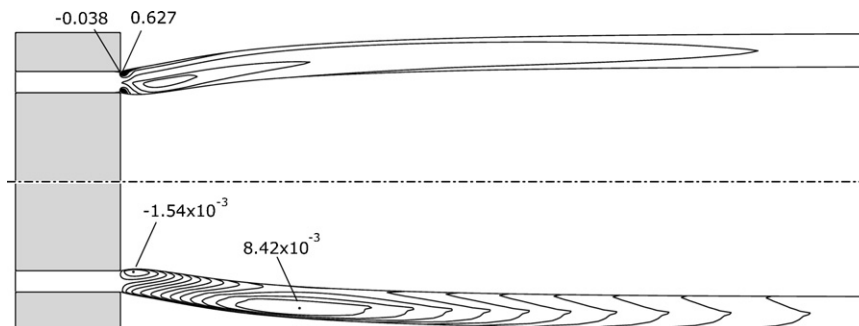


Fig. 18. Contour plots of  $\tau_{prr}$ , upper half, and  $\tau_{p00}$ , lower half, for  $Wi=4$ ,  $\varepsilon=0.02$ ,  $\beta=0.9$ ,  $a=0.8$ ,  $l_1=1$ ,  $l_2=50$ . (For clarity we show the region  $0 \leq z \leq 8$ ).

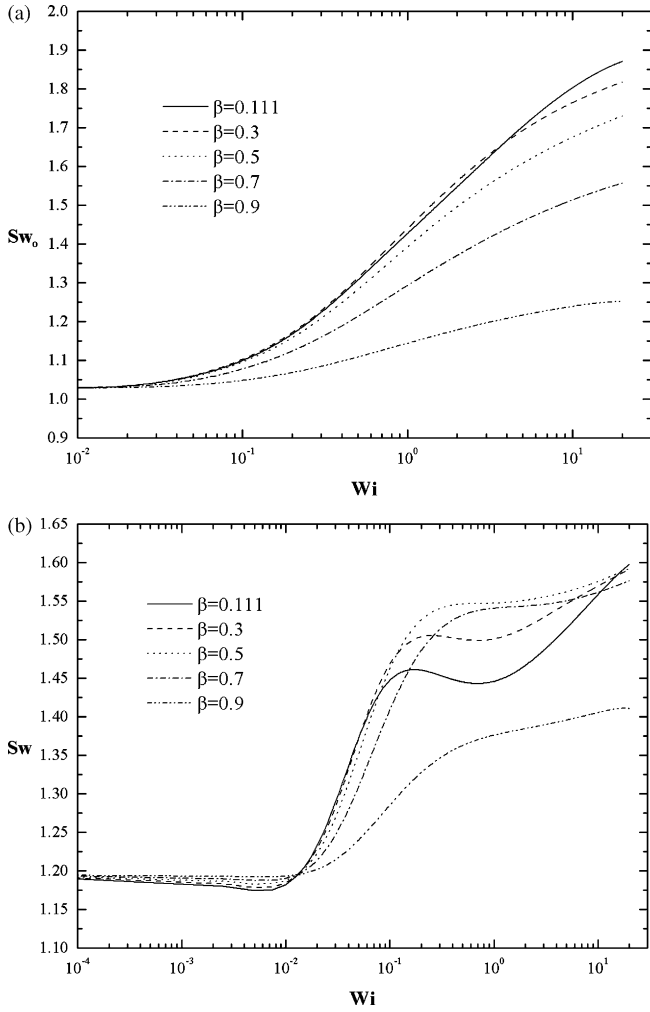


Fig. 20. Dependence of (a) the outer radius, and (b) the thickness swell ratio on the  $Wi$  number for  $\varepsilon = 0.05$ ,  $\alpha = 0.9$ ,  $l_1 = 1$ ,  $l_2 = 50$  and various  $\beta$ .

4.2.4. Effect of the elongation parameter,  $\varepsilon$

Another significant parameter characterizing the flow of PTT fluids is the elongation parameter,  $\varepsilon$ , because it controls the level of the elongational viscosity, and as it approaches zero, the elongation viscosity increases to infinity. The influence of this parameter is more involved because it also affects the shear viscosity of the fluid. In order to study its influence on the flow at hand we have plotted in Fig. 22 the contour lines of  $\tau_{pzz}$  (upper half) and  $\tau_{prz}$  (lower half) for  $Wi = 2.5$ ,  $\varepsilon = 0.05$ ,  $\beta = 0.3$ ,  $a = 0.7$ ,  $l_1 = 1.5$ ,  $l_2 = 25$ . Comparing them

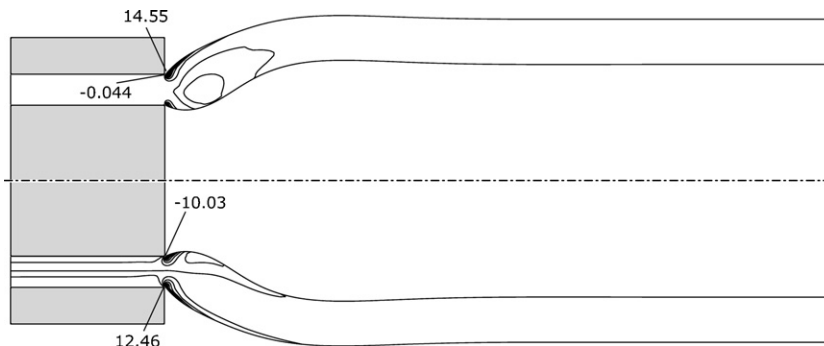


Fig. 22. Contour plots of  $\tau_{pzz}$ ,  $\tau_{prz}$  on the upper and lower half, respectively for  $Wi = 2.5$ ,  $\varepsilon = 0.05$ ,  $\beta = 0.3$ ,  $a = 0.7$ ,  $l_1 = 1.5$ ,  $l_2 = 25$ . (For clarity we show the region  $0 \leq z \leq 8$ ).

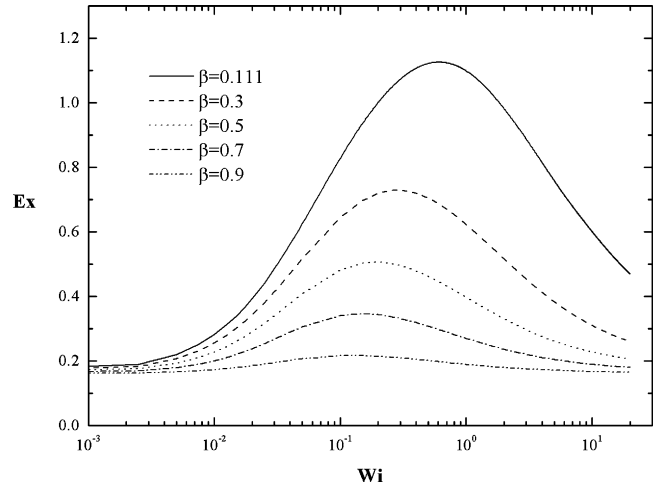


Fig. 21. Dependence of the exit pressure losses on the  $Wi$  number for  $\varepsilon = 0.05$ ,  $\alpha = 0.9$ ,  $l_1 = 1$ ,  $l_2 = 50$  and various  $\beta$ .

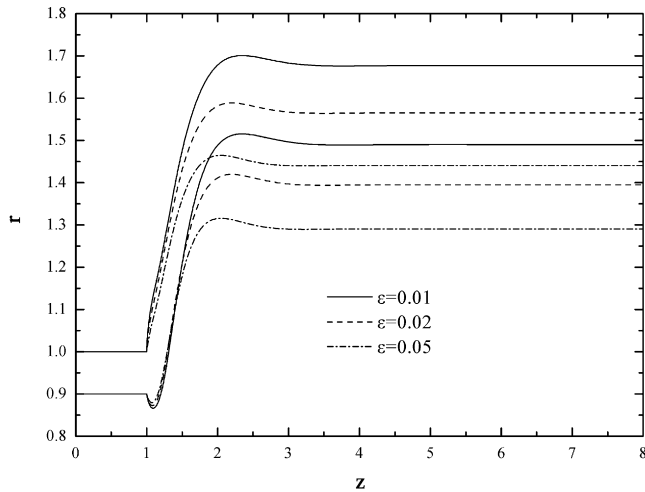
with those in Fig. 14, where the only parameter that is different is  $\varepsilon$ , we find that the maximum values of both  $\tau_{pzz}$  and  $\tau_{prz}$  have decreased now, since both elongation and shear viscosity decrease as  $\varepsilon$  increases.

Fig. 23 gives the shapes of the free surfaces for a fixed  $Wi$  number ( $Wi = 1$ ) and various values of  $\varepsilon$ . The rest of the parameters are  $\beta = 0.3$ ,  $a = 0.9$ ,  $l_1 = 1$ ,  $l_2 = 30$ . Clearly the extrudate swelling decreases as  $\varepsilon$  increases and both the elongation and shear viscosity of the fluid decrease. This can be seen even more clearly in Fig. 24 which depicts the two swelling ratios as a function of  $Wi$  and for three different values of  $\varepsilon$ . The outer radius swell,  $Sw_o$ , decreases with increasing  $\varepsilon$ , for all  $Wi$ .  $Sw_i$  behaves qualitatively the same except that it slightly increases with  $\varepsilon$  for  $0.03 \leq Wi \leq 0.25$ . Finally the thickness swell ratio decreases for all  $Wi$  numbers as  $\varepsilon$  increases and depends non-monotonically on  $Wi$ .

The effect of the elongation parameter on the exit pressure losses is presented in Fig. 25. Clearly, the pressure drop decreases with  $\varepsilon$  for all values of  $Wi$  because of the increased shear thinning that this parameter introduces to the PTT model.

4.2.5. Effect of the die opening

The final parameter that can affect the extrudate is the opening of the annular die. In order to examine its influence, various simulations were performed varying the geometric ratio  $a$ . In this case it is easier to draw quantitative conclusions by depicting the swelling ratios, for example, as a function of  $Wi_\delta$ , the Weissenberg number based on the annular die gap,  $\delta$ .



**Fig. 23.** Shape of the calculated free surfaces of the annular extrudate for  $Wi = 1$ ,  $\beta = 0.3$ ,  $a = 0.9$ ,  $l_1 = 1$ ,  $l_2 = 30$  and various  $\varepsilon$ .

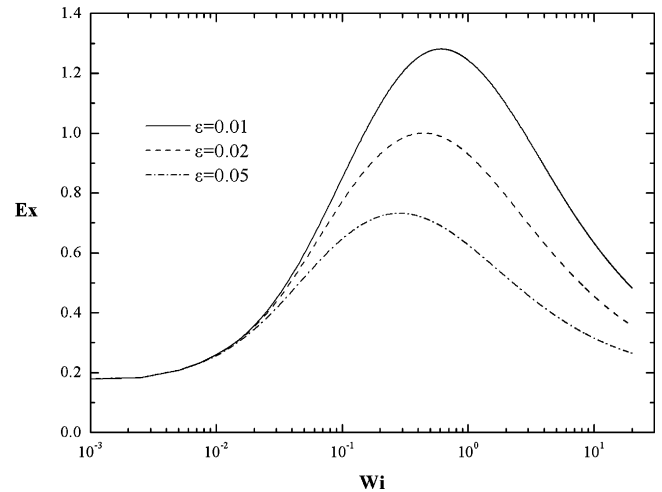


**Fig. 25.** Dependence of the exit pressure losses on the  $Wi$  number for  $\beta = 0.3$ ,  $a = 0.9$ ,  $l_1 = 1$ ,  $l_2 = 30$  and various  $\varepsilon$ .

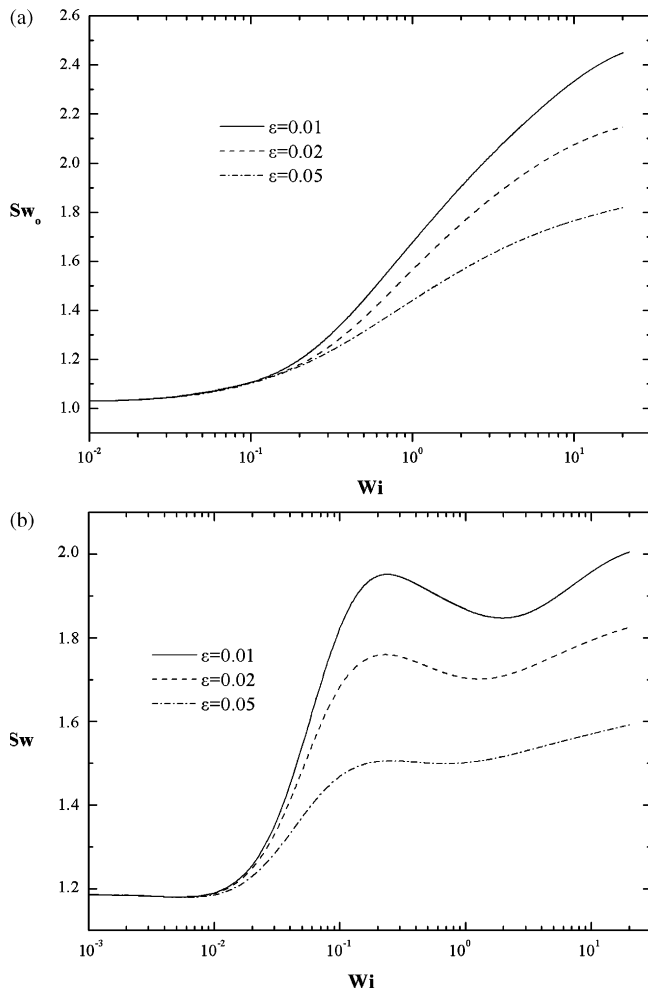


**Fig. 24.** Dependence of (a) the outer radius and (b) the thickness swell ratio on the  $Wi$  number for  $\beta = 0.3$ ,  $a = 0.9$ ,  $l_1 = 1$ ,  $l_2 = 30$  and various  $\varepsilon$ .

To study the effect of the annular die geometry on the stresses we plotted in Fig. 26 the contour lines of  $\tau_{pzz}$  (upper half) and  $\tau_{prz}$  (lower half) for  $\varepsilon = 0.02$ ,  $\beta = 0.3$ ,  $a = 0.8$ ,  $l_1 = 1$ ,  $l_2 = 30$  and for  $Wi = 2$  which corresponds to  $Wi_\delta = 10$ , a value that is the same with that in Fig. 14. Comparing these two figures we can see that the maximum values of the axial as well as the shear stress have increased due to the smaller die gap. However the swelling does not seem to have been influenced much. In order to examine more completely the dependence of the swelling on the geometric ratio,  $a$ , we have plotted in Fig. 27 the two swelling ratios. It can be observed that for either the lowest or the highest values of  $Wi_\delta$  the swelling ratio of the outer radius (same for the inner one) remains roughly the same. In the first case the material behaves nearly as Newtonian and in the latter the  $Wi_\delta$  is so high that shear thinning increases and hides the influence of the increased shear rate as the die opening decreases. For intermediate values of  $Wi_\delta$  the swelling ratio of the outer radius tends to decrease with  $a$ . On the contrary the thickness swell ratio increases with  $a$ , for low and intermediate values of  $Wi_\delta$ , while for higher values of  $Wi_\delta$  it remains roughly the same. The effect of  $Wi$  on all three swelling ratios is monotonic given the rest of the parameter values.

Finally Fig. 28 presents the dependence of the exit pressure losses on the radius ratio of the annular die. Clearly for the range of the radius ratios studied, the pressure loss for a given  $Wi_\delta$  number does not change much with  $a$ , though for moderate to high values of  $Wi_\delta$  a slight increase for  $a = 0.95$  is observed. Once more, it is seen that  $Wi_\delta$  affects non-monotonically  $Ex$ , as it increases  $Wi_\delta < 3$  and then it sharply decreases. This is because of its dual role: it increases both the material elasticity and its shear thinning behavior. The same can be seen in Fig. 25.

#### 4.2.6. Comparison with experiments

It is important to compare results of our numerical viscoelastic simulations with existing experimental ones and, simultaneously, examine the capability of the PTT model to predict complex flows of existing polymers. Orbey and Dealy [39] carried out an experimental investigation on the parison swelling of high-density polyethylene (HDPE) melts for various die geometries. In their experiments three different HDPE resins have been used for which viscometric data were obtained for the shear viscosity and first normal stress difference at 170 °C. These are shown in Fig. 29 along with their fit as obtained from the exponential PTT model with  $\varepsilon = 0.03$ ,  $\xi_s = 0$ ,  $\lambda = 5s$ ,  $\mu_p = 32000 \text{ Pa s}$  and  $\mu_s = 300 \text{ Pa s}$ . These parameter values resulted from a simple (not fully optimized) trial and error

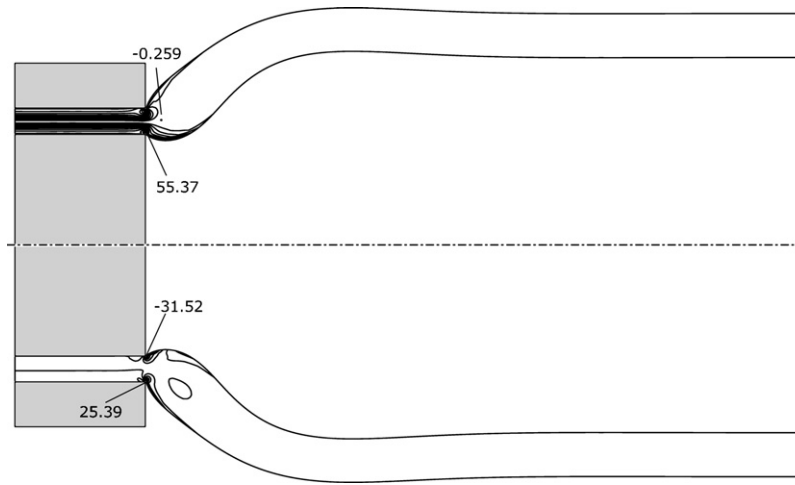


Fig. 26. Contour plots of  $\tau_{pzz}$ , upper half, and  $\tau_{prz}$ , lower half, for  $Wi = 2$ ,  $\varepsilon = 0.02$ ,  $\beta = 0.3$ ,  $a = 0.8$ ,  $l_1 = 1$ ,  $l_2 = 30$ . (For clarity we show the region  $0 \leq z \leq 6$ ).

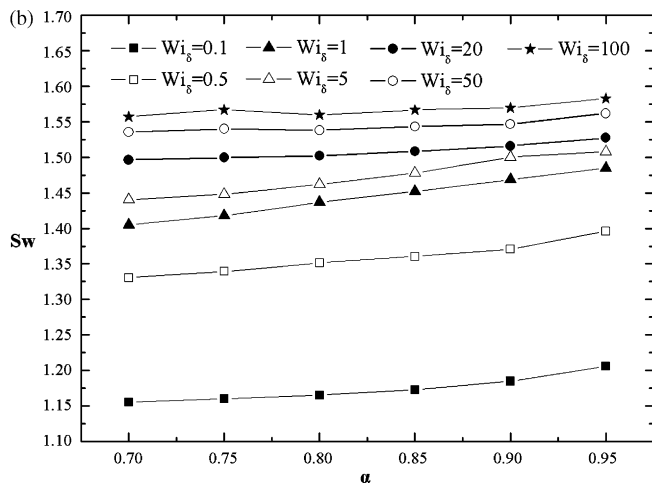
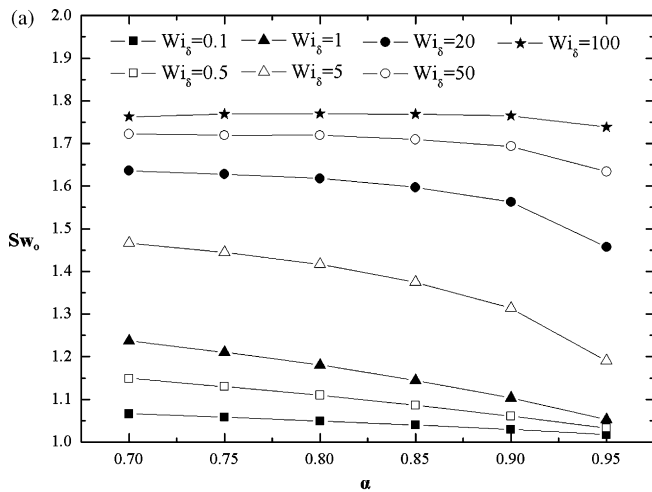


Fig. 27. Dependence of (a) the outer radius and (b) the thickness swell ratio on the radius ratio of the annular die,  $a$ , for  $\varepsilon = 0.05$ ,  $\beta = 0.3$ ,  $a = 0.9$ ,  $l_1 = 1$ ,  $l_2 = 50$  and various values of  $Wi_\delta$ .

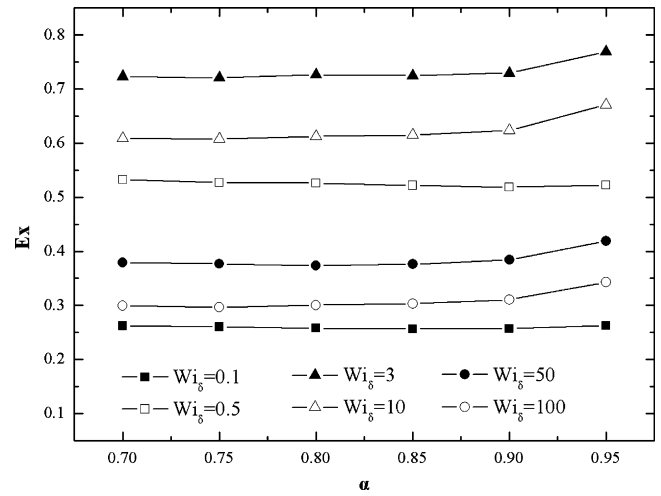


Fig. 28. Dependence of the exit pressure losses on the radius ratio of the annular die,  $a$ , for  $\varepsilon = 0.05$ ,  $\beta = 0.3$ ,  $a = 0.9$ ,  $l_1 = 1$ ,  $l_2 = 50$  and various values of  $Wi_\delta$ .

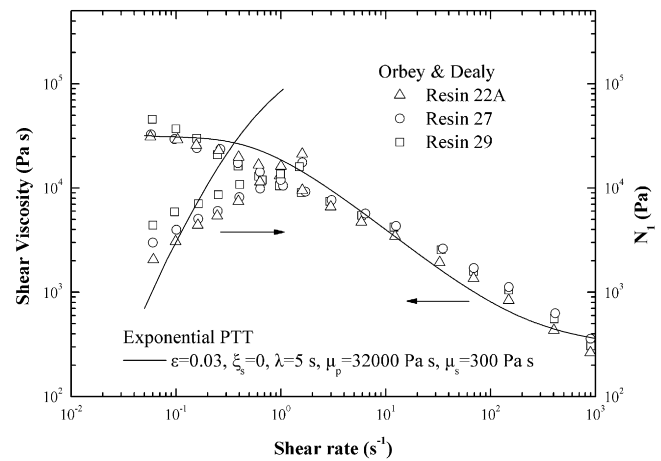


Fig. 29. Shear viscosity and first normal stress difference data for HDPE melts at 170 °C, from the experiments by Orbey and Dealy [39], along with predictions of the same properties using a single-mode, affine PTT model with parameter values resulting from a simple trial-and-error fit to the data.

**Table 5**

Comparison of the predictions of the outer radius, thickness ratios and the exit pressure correction with previous numerical and experimental studies for HDPE melts

		$Q=0.024\text{ cm}^3/\text{s}$		$Q=0.095\text{ cm}^3/\text{s}$		$Q=0.238\text{ cm}^3/\text{s}$	
		$Sw_o$	$Sw$	$Sw_o$	$Sw$	$Sw_o$	$Sw$
Orbey and Dealy [39]	22A	1.33	1.26	1.39	1.28	1.46	1.34
	27	1.39	1.54	1.66	1.72	1.71	1.79
	29	–	–	1.51	1.58	1.56	1.75
Luo and Mitsoulis [5]		1.30	1.54	1.46	1.79	1.57	2.05
Present work		1.279	1.462	1.493	1.398	1.547	1.404

numerical procedure. The resulting viscosity ratio is  $\beta=0.0093$ , a very small value, which in essence implied that the solvent contribution to shear viscosity is negligible. This is expected to make the simulations of the process particularly challenging. Considering the fact that only one relaxation time is used to obtain the viscometric data of these fluids, one can conclude that the comparison between the predictions of the PTT model and the experimental data is quite satisfactory. Obviously a better agreement would be obtained if we had used a spectrum with several relaxation times.

The annular gap of the straight die which was used by Orbey and Dealy [39] is 1.5875 mm and the outer radius is 6.35 mm which corresponds to radii ratio  $\alpha=0.75$ . In Table 5 we present our numerical predictions for the outer radius as well as the thickness ratio along with the experimental data of Orbey and Dealy [39] and the predictions of Luo and Mitsoulis [5]. Given that there are no adjustable parameters, but only the viscometric data have been used, the overall agreement between our numerical predictions and the experimental data is good. The extremely low value of  $\beta$  and the rather low value of  $\varepsilon$  lead to no convergence of the algorithm for the three highest values of flow rate in the experiments, which correspond to  $Wi=6.75$ , 13.49 and 33.73. We should note here, however, that there is a small discrepancy in the qualitative behavior of the predicted thickness ratio. We observe that for the smallest flow rate,  $0.024\text{ cm}^3/\text{s}$ , the predicted thickness ratio takes its largest value, although in the experiments, increase of the flow rate always resulted in an increase of the thickness ratio. However we have already seen in Fig. 20 that the variation of the thickness ratio for the lowest value of solvent viscosity ratio ( $\beta=0.111$ ) is not a monotonic function of  $Wi$ , which for a given relaxation time and geometry is proportional to the flow rate. Luo and Mitsoulis [5] have also predicted this change of monotonicity, although for larger values of the flow rate. We could possibly attribute this discrepancy to the inadequacy of our model to predict more accurately the normal stresses and the fact that we have included in it a single relaxation time.

## 5. Concluding remarks

The steady extrusion from an annular die of a viscoelastic fluid following the PTT constitutive law has been studied. The mixed finite element method has been combined with a quasi-elliptic mesh generation scheme, which allows accurately capturing large deformations of the free surfaces of the fluid as it exits the die. Simulations up to high Weissenberg numbers were successful by using the EVSS-G method for the calculation of the elastic stresses together with the SUPG method for the weighting of the constitutive equations. It was found to be essential to couple the entire problem (the velocity and stress fields with the location of the mesh nodes) for obtaining solutions at such high  $Wi$  numbers.

Studying the fully developed flow in the straight annular die revealed the important role that the solvent viscosity can play in addition to the fluid elasticity and extensional viscosity. Indeed the

presence of a Newtonian solvent may lead to a nonmonotonic variation of the velocity profiles as the Weissenberg number increases. Results from a complete parametric analysis have been presented for the fully developed flow inside an annular die as well as for the extrusion through such a die. The effects of fluid elasticity, the elongation parameter of the PTT model which is also related with its shear thinning behavior and the solvent viscosity on this process have been thoroughly examined. The swelling of the extrudate increases with  $Wi$ , although for high values of  $Wi$  its rate of increase is diminished since shear thinning becomes significant. As for the exit pressure losses, they increase initially with  $Wi$  reaching a maximum at moderate values of  $Wi$ , decreasing however after this point because of shear thinning. Increasing the ratio of the solvent viscosity over the total viscosity,  $\beta$ , increases the Newtonian character of the material decreasing the extrudate swelling. The magnitude of the elastic stresses as well as the swelling of the extrudate and the exit pressure losses decrease with increasing the elongation parameter,  $\varepsilon$ , since the latter reduces the elongation and shear viscosities of the PTT fluid. In order to compare our model predictions with the experimental data available in the literature for three HDPE resins, the only three parameters of the single-mode PTT model were determined by fitting through trial and error. These parameters were then used in our numerical algorithm to predict the extrudate geometry. Our results compared favorably to the experimental ones and those obtained by solving an integral constitutive model with eight modes.

## Acknowledgement

This work was partially supported under the PENED program (Grant number 136, starting year 2001) of the General Secretariat of Research and Technology of the Ministry of Development of Greece.

## References

- [1] A. Garcia-Rejon, R.W. DiRaddo, M.E. Ryan, Effect of die geometry and flow characteristics on viscoelastic annular swell, *J. Non-Newton. Fluid Mech.* 60 (1995) 107–128.
- [2] J.R.A. Pearson, R. Trottnow, On die swell: some theoretical results, *J. Non-Newton. Fluid Mech.* 4 (1978) 195–215.
- [3] R.I. Tanner, A theory of die swell, *J. Polym. Sci. A2* (8) (1970) 2067–2078.
- [4] M.J. Crochet, R. Keunings, Die swell of a Maxwell fluid: numerical prediction, *J. Non-Newton. Fluid Mech.* 7 (1980) 199–212.
- [5] X.-L. Luo, E. Mitsoulis, Memory phenomena in extrudate swell simulations for annular dies, *J. Rheol.* 33 (1989) 1307–1327.
- [6] J.M. Marchal, M.J. Crochet, A new mixed finite element for calculating viscoelastic flow, *J. Non-Newton. Fluid Mech.* 26 (1987) 77–114.
- [7] Y. Seo, Some studies of annular extrudate swell phenomena, *J. Appl. Polym. Sci.* 41 (1990) 25–38.
- [8] Y.-C. Ahn, M.E. Ryan, Analysis of extrudate swell from an annular die, *Comput. Fluids* 21 (1992) 267–289.
- [9] S. Tanoue, T. Kajiwara, Y. Iemoto, K. Funatsu, High Weissenberg number simulation of an annular extrudate swell using the differential type constitutive equation, *Polym. Eng. Sci.* 38 (1998) 409–419.
- [10] S. Tanoue, Y. Iemoto, Effect of die gap width on annular extrudates by the annular extrudate swell simulation in steady states, *Polym. Eng. Sci.* 39 (1999) 2172–2180.
- [11] Y. Otsuki, T. Kajiwara, K. Funatsu, Numerical simulations of annular extrudate swell of polymer melts, *Polym. Eng. Sci.* 37 (1997) 1171–1181.
- [12] Y. Otsuki, T. Kajiwara, K. Funatsu, Numerical simulations of annular extrudate swell using various types of viscoelastic models, *Polym. Eng. Sci.* 39 (1999) 1969–1981.
- [13] E. Mitsoulis, Annular extrudate swell of pseudoplastic and viscoplastic fluids, *J. Non-Newton. Fluid Mech.* 141 (2007) 138–147.
- [14] K. Housiadas, G. Georgiou, J. Tsamopoulos, The steady annular extrusion of a Newtonian liquid under gravity and surface tension, *Int. J. Numer. Methods Fluids* 33 (2000) 1099–1119.
- [15] K. Housiadas, J. Tsamopoulos, Unsteady extrusion of a viscoelastic annular film. Part I. General model and its numerical solution, *J. Non-Newton. Fluid Mech.* 88 (2000) 229–259.
- [16] K. Housiadas, J. Tsamopoulos, Unsteady extrusion of a viscoelastic annular film. Part II. Linearized model and its analytical solution, *J. Non-Newton. Fluid Mech.* 88 (2000) 303–325.

- [17] G. Georgiou, Annular liquid jets at high Reynolds numbers, *Int. J. Numer. Methods Fluids* 42 (2003) 117–130.
- [18] Y. Dimakopoulos, J. Tsamopoulos, A quasi-elliptic transformation for moving boundary problems with large anisotropic deformations, *J. Comp. Phys.* 192 (2003) 494–522.
- [19] G. Karapetsas, J. Tsamopoulos, Transient squeeze flow of viscoplastic materials, *J. Non-Newton. Fluid Mech.* 133 (2006) 35–56.
- [20] Y. Dimakopoulos, J. Tsamopoulos, Transient displacement of a Newtonian fluid by air in straight or suddenly constricted tubes, *Phys. Fluids* 15 (7) (2003) 1973–1991.
- [21] Y. Dimakopoulos, J. Tsamopoulos, On the gas-penetration in straight tubes completely filled with a viscoelastic fluid, *J. Non-Newton. Fluid Mech.* 117 (2–3) (2004) 117–139.
- [22] Y. Dimakopoulos, J. Tsamopoulos, Transient displacement of Newtonian and viscoplastic liquids by air from complex conduits, *J. Non-Newton. Fluid Mech.* 142 (1–3) (2007) 162–182.
- [23] K. Foteinopoulou, V. Mavrantzas, Y. Dimakopoulos, J. Tsamopoulos, Numerical simulation of multiple bubbles growing in a Newtonian liquid filament undergoing stretching, *Phys. Fluids* 18 (042106) (2006) 1–24.
- [24] J. Tsamopoulos, Y. Dimakopoulos, N. Chatzidai, G. Karapetsas, M. Pavlidis, Steady bubble rise and deformation in Newtonian and viscoplastic fluids and conditions for their entrapment, *J. Fluid Mech.* 601 (2008) 123–164.
- [25] N. Phan-Thien, R.I. Tanner, A new constitutive equation derived from network theory, *J. Non-Newton. Fluid Mech.* 2 (1977) 353–365.
- [26] N. Phan-Thien, A nonlinear network viscoelastic model, *J. Rheol.* 22 (1978) 259–283.
- [27] X.L. Luo, R.I. Tanner, A Streamline element scheme for solving viscoelastic flow problems. Part I. Differential constitutive equations, *J. Non-Newton. Fluid Mech.* 21 (1986) 179–199.
- [28] D. Rajagopalan, R.C. Armstrong, R.A. Brown, Finite element methods for calculation of steady, viscoelastic flow using constitutive equations with Newtonian viscosity, *J. Non-Newton. Fluid Mech.* 36 (1990) 159–192.
- [29] R.A. Brown, M.J. Szady, P.J. Northey, R.C. Armstrong, On the numerical stability of mixed finite-element methods for viscoelastic flows governed by differential constitutive equations, *Theor. Comput. Fluid Dyn.* 5 (1993) 77–106.
- [30] T.J. Chung, *Computational Fluid Dynamics*, Cambridge University Press, Cambridge, 2002, pp. 533–580.
- [31] G. Karapetsas, A study on time-dependent and unstable under conditions flows of viscoplastic and viscoelastic fluids, Ph.D. Thesis, University of Patras, 2007.
- [32] A.N. Brooks, T.J.R. Hughes, Streamline upwind/Petrov-Galerkin formulations for convection dominated flows with particular emphasis on the incompressible Navier–Stokes equations, *Comput. Methods Appl. Mech. Eng.* 32 (1982) 199–259.
- [33] H.A. van der Vorst, Bi-CGSTAB: a fast and smoothly converging variant of Bi-CG for the solution of nonsymmetrical linear systems, *SIAM, J. Sci. Stat. Comput.* 13 (1992) 631–644.
- [34] O. Schenk, K. Gärtner, Solving unsymmetric sparse systems of linear equations with PARDISO, *J. Future Gener. Comput. Syst.* 20 (2004) 475–487.
- [35] O. Schenk, K. Gärtner, On fast factorization pivoting methods for symmetric indefinite systems, *Elec. Trans. Numer. Anal.* 23 (2006) 158–179.
- [36] F.T. Pinho, P.J. Oliveira, Axial annular flow of a nonlinear viscoelastic fluid—an analytical solution, *J. Non-Newton. Fluid Mech.* 93 (2000) 325–337.
- [37] D.O.A. Cruz, F.T. Pinho, P.J. Oliveira, Analytical solutions for fully developed laminar flow of some viscoelastic liquids with a Newtonian solvent contribution, *J. Non-Newton. Fluid Mech.* 132 (2005) 28–35.
- [38] P.J. Oliveira, F.T. Pinho, Analytical solution for fully developed channel and pipe flow of Phan-Tien Tanner fluids, *J. Fluid Mech.* 387 (1999) 271–280.
- [39] N. Orbey, J.M. Dealy, Isothermal swell of extrudate from annular dies; effects of die geometry, flow rate, and resin characteristics, *Polym. Eng. Sci.* 24 (1984) 511–518.